

1 **Nucleoid size scaling and intracellular organization of translation** 2 **across bacteria**

3

4 William T. Gray^{1,2,7}, Sander K. Govers^{1,3,7}, Yingjie Xiang^{1,3}, Bradley R. Parry^{1,3}, Manuel Campos^{1,3,5},
5 Sangjin Kim^{1,4}, and Christine Jacobs-Wagner^{1,3,4,6,8,*}.

6

7 ¹Microbial Sciences Institute, Yale University, West Haven, CT, USA

8 ²Department of Pharmacology, Yale University, New Haven, CT, USA

9 ³Department of Molecular, Cellular and Developmental Biology, Yale University, New Haven, CT,
10 USA

11 ⁴Howard Hughes Medical Institute, Yale University, New Haven, CT, USA

12 ⁵Laboratoire de Microbiologie et Génétique Moléculaires, Centre de Biologie Intégrative, Centre
13 National de la Recherche Scientifique, Université de Toulouse, UPS, Toulouse, France

14 ⁶Department of Microbial Pathogenesis, Yale School of Medicine, New Haven, CT, USA

15

16 ⁷These authors contributed equally

17

18 ⁸Lead contact

19

20 *Correspondence: Christine.Jacobs-Wagner@yale.edu.

21

22 **Summary**

23 The scaling of organelles with cell size is thought to be exclusive to eukaryotes. Here, we
24 demonstrate that similar scaling relationships hold for the nucleoid in bacteria. Despite the
25 absence of a nuclear membrane, nucleoid size strongly correlates with cell size, independent of
26 changes in DNA amount and across various nutrient conditions. This correlation is observed in
27 diverse bacteria, revealing a near-constant ratio between nucleoid and cell size for a given
28 species. As in eukaryotes, the nucleocytoplasmic ratio in bacteria varies greatly among species.
29 This spectrum of nucleocytoplasmic ratios is independent of genome size, and instead appears
30 linked to the average cell size of the population. Bacteria with different nucleocytoplasmic ratios
31 have different biophysical properties of the cytoplasm, impacting the mobility and localization of
32 ribosomes. Together, our findings identify new organizational principles and biophysical features
33 of bacterial cells, implicating the nucleocytoplasmic ratio and cell size as determinants of the
34 intracellular organization of translation.

35

36 **Keywords**

37 Nucleoid, nucleocytoplasmic ratio, scaling properties, cell size, ribosome mobility, intracellular
38 organization.

39

40 **Introduction**

41 The spatial organization of the cell has a profound effect on various cellular processes from
42 bacteria to humans (Bisson-Filho et al., 2018; Diekmann and Pereira-Leal, 2013; Harold, 2005;
43 Surovtsev and Jacobs-Wagner, 2018). In eukaryotic cells, a distinctive feature of intracellular
44 organization is the nucleus, a membrane-enclosed organelle that harbors most of the cell's genetic
45 material. The nuclear envelope hereby spatially confines the genetic material and physically
46 separates transcription and translation. While the sizes of cells and nuclei vary considerably
47 among species and tissues, there is a remarkable linear size scaling relationship between the cell
48 and the nucleus for a given cell type, which was first reported over 100 years ago (Conklin, 1912;
49 Woodruff, 1913). Correlations between cell size and nuclear size are not only widespread among
50 eukaryotic cells but also robust to genetically- and nutritionally-induced cell size perturbations
51 (Jorgensen et al., 2007; Neumann and Nurse, 2007). This scaling property results in a constant
52 ratio between nuclear and cellular volumes, also known as the karyoplasmic or
53 nucleocytoplasmic (NC) ratio (Wilson, 1925). Why cells maintain a specific NC ratio is generally
54 not well understood, though alterations in NC ratios have been associated with aging and diseases
55 such as cancer (Capell and Collins, 2006; Chow et al., 2012; Prokocimer et al., 2009; Zink et al.,
56 2004). The sizes of other cellular components such as vacuoles, mitotic spindles, centrosomes
57 and mitochondria have also been shown to scale with cell size in various eukaryotic cell types
58 (Levy and Heald, 2012; Marshall, 2015; Reber and Goehring, 2015). As such, these scaling
59 properties are believed to be unique to eukaryotes.

60

61 In bacteria, the chromosomal DNA typically occupies a subcellular region called the nucleoid
62 (Kellenberger et al., 1958; Mason and Powelson, 1956). Recently, we showed that the average
63 size of the nucleoid scales with the average size of the cell across ~4,000 gene-deletion mutants
64 of *Escherichia coli* (Campos et al., 2018). In addition, nucleoid size and cell size in *E. coli* correlate
65 at the single-cell level, at least under specific growth conditions (Junier et al., 2014; Paintdakhi et
66 al., 2016). An intuitive explanation for these observations may be linked to differences in DNA
67 amount. Even under nutrient-poor conditions, DNA replication happens during a large part of the
68 cell cycle, such that bigger cells tend to contain more DNA. This is exacerbated under nutrient-
69 rich conditions under which *E. coli* displays overlapping DNA replication cycles (Cooper and
70 Helmstetter, 1968). This leads to a continuous increase in DNA content from cell birth to division

71 (Cooper and Helmstetter, 1968). Recent work with mutants of altered cell widths further suggests
72 that the amount of DNA in such rapidly growing cells is directly coupled to cell volume (Shi et al.,
73 2017). However, whether the scaling of nucleoid size with cell size is exclusively linked to changes
74 in DNA content remains to be established. It is also currently unclear whether a scaling
75 relationship between nucleoid and cell size is robust across growth conditions or widespread
76 among bacteria. At the same time, it is unclear whether the size of the nucleoid or the volume
77 fraction it occupies within the cell has any physiological consequence. We address all of these
78 unknowns below.

79

80 **Results**

81 **Nucleoid size scaling is robust across a wide range of cell sizes in *E. coli***

82 Given that different nutrient conditions give rise to cells of different sizes (Pierucci, 1978;
83 Schaechter et al., 1958), we used phase contrast and fluorescence microscopy to examine how
84 cell size variation in exponentially growing *E. coli* may affect nucleoid size across 30 nutrient
85 conditions (M9 medium supplemented with different carbon sources \pm casamino acids and
86 thiamine, see Table S1). Cell contours were detected and curated in an automated fashion using
87 the open source software package Oufiti (Paintdakhi et al., 2016) and a support vector machine
88 model (see STAR Methods). For each condition, the areas of thousands of cells were quantified
89 from the cell contours (Figure 1A, Figure S1A). DAPI-stained nucleoids were detected using the
90 objectDetection module of Oufiti, from which we extracted the total area occupied by the DAPI
91 signal (Figure 1A). Since estimation of the nucleoid area can vary with the chosen Oufiti
92 parameters (e.g., contour rigidity, relative signal threshold), we used the same parameter values
93 across growth conditions.

94

95 Using this methodology, we observed a strong correlation (Kendall correlation $\tau \geq 0.77$) between
96 the cell area and nucleoid area of individual cells within all 30 tested growth conditions (Figure
97 1B). These results show that the nucleoid size scaling property is robust across a wide range of
98 growth rates, with doubling times varying from ~ 40 min to ~ 4 h (Figure S1B). For each condition,
99 the nucleocytoplasmic (NC) ratio (nucleoid area divided by cell area) was independent of the total
100 or normalized intensity of the DAPI signal per cell (Figure S2), and was therefore unaffected by
101 variations in DAPI staining efficiency. Moreover, we observed identical scaling relationships
102 between nucleoid and cell area for nucleoids labeled with an mCherry or CFP fusion to a subunit
103 of the nucleoid-associated HU complex (Figure S3A-C). The scaling between the cell area and the
104 total nucleoid area was preserved in filamentous cells obtained by treatment with cephalixin
105 (Figure S3D), a drug that inhibits cells division without affecting growth and DNA replication

106 (Boye and Lobner-Olesen, 1991; Rolinson, 1980). The scaling relationship in these filamentous
107 cells was almost indistinguishable from that in untreated cells (Figure S3D). These observations
108 indicate that nucleoid size scaling occurs independently of cell division and persists across a wide
109 range of cell sizes and growth conditions.

110

111 At the population level, we also observed a strong correlation ($\tau = 0.86$) between the mean cell
112 area and the mean nucleoid area of untreated cells across the tested 30 growth conditions (Figure
113 1C). This relationship was not perfectly linear, as the average NC ratio slightly decreased with
114 increasing average cell size (Figure 1C, inset). This small decrease, which will be addressed later,
115 was not a consequence of differences in growth medium osmolality (Figure S1C), which can cause
116 variations in nucleoid morphology (Cagliero and Jin, 2013).

117

118 **Nucleoid size scaling is independent of DNA replication**

119 We next investigated whether changes in DNA content underlie the scaling of nucleoid size with
120 cell size by using nutrient-poor growth conditions. In such environments, *E. coli* cells display
121 discrete cell cycle periods, known as the B, C, and D periods, corresponding to cell-cycle phases
122 before, during, and after DNA replication, respectively (Cooper and Helmstetter, 1968). If DNA
123 replication was solely responsible for nucleoid size scaling, we would expect to observe a
124 correlation between nucleoid and cell size only during the C period, and not during the B and D
125 periods when the DNA amount does not change. As cell size and the DAPI signal intensity did not
126 provide sufficient resolution to distinguish between cells in the B, C, and D periods (Figure S4A),
127 we used a strain producing a SeqA-mCherry fusion. SeqA associates with newly replicated DNA
128 by transiently binding hemi-methylated GATC sites (Brendler et al., 1995; Lu et al., 1994; Slater
129 et al., 1995). When fluorescently tagged, SeqA forms bright fluorescent foci that trail the
130 replication forks during DNA replication (C period). In the absence of DNA replication (B and D
131 periods), SeqA-mCherry displays diffuse nucleoid-associated fluorescence (Adiciptaningrum et
132 al., 2015; Helgesen et al., 2015; Molina and Skarstad, 2004; Wallden et al., 2016) (Figure 2A). By
133 quantifying the relative area of the SeqA-mCherry signal and combining this information with cell
134 area measurements, we were able to identify three distinct groups of cells—corresponding to the
135 B, C, and D cell cycle periods—in populations growing under various nutrient-poor conditions
136 (Figure 2A and Figure S4B-D). Surprisingly, we found a strong correlation of nucleoid area with
137 cell area for all three periods (Figure 2B and Figure S4D). The correlations and slopes were the
138 strongest in the C period under all 11 tested nutrient-poor conditions, but both remained
139 significant during the B and D periods (Figure 2B and Figure S4B-C). Apart from these small
140 differences between cell cycle periods, we observed similar average NC ratios for each growth

141 condition (Figure S4B). These results indicate that the scaling between nucleoid and cell sizes
142 occurs independently of DNA replication.

143

144 To confirm this unexpected conclusion, we used temperature-sensitive *dnaC2* mutant cells
145 producing an HU-mCherry fusion to visualize the nucleoids. At restrictive temperatures, these
146 cells are unable to initiate new rounds of DNA replication, but continue to grow without dividing
147 (Carl, 1970). We found that 90 min after the temperature shift to 37 °C, the average cell size of
148 the population began increasing at which time we measured the size of both cells and nucleoids
149 at regular intervals for 210 min. Remarkably, the size of the nucleoid increased with cell size over
150 an almost 4-fold range before reaching a plateau in long cells (Figure 2C-D). Before reaching this
151 limit, the scaling relationship in the absence of DNA replication was similar to that observed
152 under the permissive temperature (30 °C) when DNA replication occurs (Figure 2C-D). Together,
153 these observations demonstrate that nucleoid size scaling occurs irrespective of changes in DNA
154 content.

155

156 **The nucleoid size scaling property is conserved in *Caulobacter crescentus*, but with** 157 **a different NC ratio**

158 To examine whether a scaling relationship between nucleoid and cell size is observed in other
159 bacteria, we imaged DAPI-stained *C. crescentus* cells expressing CFP-labeled DnaN. DnaN is the β
160 sliding clamp of the DNA polymerase, which, when fluorescently labeled, forms foci during DNA
161 replication but otherwise displays a disperse distribution (Arias-Cartin et al., 2017; Collier and
162 Shapiro, 2009; Fernandez-Fernandez et al., 2013). By quantifying the signal area of DnaN-CFP, we
163 were able to readily identify cells in distinct cell-cycle periods (Figure 3A). As with *E. coli* (Figure
164 2B), we observed a strong scaling relationship between nucleoid size and cell size in cells in the
165 B and D periods (Figure 3B), indicating that nucleoid size scaling occurs even in the absence of
166 DNA replication. As in *E. coli*, nucleoid size determination in *C. crescentus* was independent of
167 DAPI signal intensity (Figure S5A), and insensitive to the nucleoid labeling method (Figure S5B).
168 Scaling was maintained in defined (M2G) and complex (PYE) growth media (Figure S5C) as well
169 as in mutants with altered cell sizes and morphologies (Figure S5D-E), such as FtsZ-depleted,
170 $\Delta rodZ$ and Δhfq cells (Alyahya et al., 2009; Irnov et al., 2017; Wang et al., 2001).

171

172 Nucleoid size scaled with cell size in both *E. coli* and *C. crescentus*. However, their NC ratios were
173 very different (Figure 3C). This is consistent with observations that the nucleoid spreads through
174 most of the cell in *C. crescentus* whereas *E. coli* displays DNA-free regions (Jensen and Shapiro,
175 1999; Kellenberger et al., 1958). The large NC ratio in *C. crescentus* was not due to PopZ-mediated

176 attachment of the chromosome to the cell poles (Bowman et al., 2008; Ebersbach et al., 2008), as
177 it was maintained in the $\Delta popZ$ mutant (Figure S5E-F).

178

179 **Nucleoid size scaling across bacterial phyla reveals a continuum of NC ratios**

180 The scaling relationship between nucleoid and cell sizes is likely a common bacterial feature, as
181 we observed it in over 35 species from different phyla or classes (Figure 4A and Figure S6A). Each
182 species investigated displayed a constant, specific NC ratio (Figure 4B). To avoid measurement
183 biases, we used the same Oufiti parameters to identify the nucleoid contour of all cells in this
184 dataset. As with *E. coli* and *C. crescentus*, we confirmed that the NC ratio was not affected by the
185 intensity of the DNA signal (Figure S7A-B). We also observed no correlation between the average
186 DNA signal intensity and the average NC ratio (Figure S7C). The various species were generally
187 grown in complex media described in the literature or recommended by the provider. In some
188 cases, we examined different growth conditions. For example, we imaged *Bacteroides*
189 *thetaiotaomicron* (*B. theta*) grown *in vitro* in both complex (TYG) and defined (GMM) media, or *in*
190 *vivo* in mono-associated gnotobiotic mice. For the latter, the samples were obtained from the
191 cecum and feces. These different growth conditions revealed differences in cell sizes but, in all
192 cases, nucleoid size scaled with cell size at the single-cell level (Figure 4A).

193

194 The name "nucleoid" (nucleus-like) comes from the early observation that the bacterial
195 chromosome occupies a distinct intracellular region (Kellenberger et al., 1958; Mason and
196 Powelson, 1956), as exemplified by the organization of the γ -proteobacterium *E. coli* (Figure 1A).
197 The near-cell-filling organization of the chromosome in the α -proteobacterium *C. crescentus* is
198 usually ignored or thought of as an exception (Campos and Jacobs-Wagner, 2013; Surovtsev and
199 Jacobs-Wagner, 2018). Analysis of the average NC ratios of our panel of diverse species revealed
200 that high average NC ratios, i.e., near-cell-filling nucleoids, can be found not only in other α -
201 proteobacteria but also in some Bacteroidetes (Figure 4B). Furthermore, there was no
202 subdivision of the analyzed bacteria into discrete lower and higher NC ratio categories. Instead,
203 we observed a continuum of average NC ratios across species (Figure 4B).

204

205 While sorting species based on their average NC ratios revealed some phylogenetic clustering
206 (Figure 4B), phylum association was not necessarily predictive of NC ratio. For example, α -
207 proteobacteria generally had a higher NC ratio than proteobacteria from the β , γ , or δ classes
208 (Figure 4B). Bacteroidetes provided a striking example of distinct chromosome organization
209 within a phylum. *Cytophaga hutchinsonii* displayed a high NC ratio, characteristic of cell-filling
210 DNA, whereas *Parabacteroides distasonis* exhibited a considerably lower NC ratio and clear DNA-
211 free regions (Figure 4B and Figure S6A). These results indicate that the intracellular organization

212 of the chromosome is an evolvable feature that varies significantly between species without strict
213 phylogenetic determinants.

214

215 **The average NC ratio negatively correlates with the average cell size**

216 Given this surprisingly large spectrum of average NC ratios among bacteria, we wondered
217 whether certain cellular characteristics are associated with a given NC ratio. We found no
218 correlation between genome size and average NC ratio (or average nucleoid area, or cell volume),
219 despite a ~3-fold difference in genome size between the included species (Figure S6B). Growth
220 rate was also a poor predictor of NC ratios. Fast-growing species such as *E. coli* (in LB), *Bacillus*
221 *subtilis* (in LB) and *B. theta* (in TYG medium), which have doubling times of ~20 to ~30 min at 37
222 °C (Eley et al., 1985; Taheri-Araghi et al., 2015; Weart et al., 2007) displayed a wide range of NC
223 ratios, whereas the NC ratio of the slower-growing *Myxococcus xanthus* (in CYE medium), which
224 has a doubling time of ~4 h (Sun et al., 1999), was similar to that of *E. coli* growing in LB.

225

226 We did, however, observe a striking, seemingly exponential relationship between the average cell
227 volume and the average NC ratio of bacteria (Figure 5A). The exponential relationship was
228 particularly apparent upon plotting the mean NC ratio versus the logarithm of the mean cell
229 volume (Figure 5A, inset), with a Kendall correlation $\tau = -0.70$. This strong correlation indicates
230 that the average cell volume of a species is highly predictive of the average NC ratio. We also
231 observed strong relationships between other morphological descriptors and the NC ratio (Figure
232 5B). Further underscoring the validity of these relationships is the fact that the *E. coli* data from
233 cultures grown under 30 different nutrient conditions (Figure 1C) overlapped almost perfectly
234 with the curve obtained with the different bacterial species (Figure 5A, inset). The negative
235 relationship between average NC ratio and average cell size observed in these experiments
236 (Figure 1C) thus appears to be a consequence of the more general relationship between these two
237 cellular characteristics.

238

239 **The cytoplasm of bacteria with different NC ratios displays different biophysical** 240 **properties**

241 What are the physiological implications of a high or low NC ratio? We speculated that DNA might
242 affect the dynamics, and thereby the organization, of large cellular components whose diffusion
243 may be impeded by the DNA meshwork. In bacteria with low NC ratios like *E. coli*, large objects
244 may be able to more freely diffuse in DNA-free regions. In contrast, motion may be limited in
245 bacteria with high NC ratios like *C. crescentus* where the DNA spreads throughout most of the
246 cytoplasm. To test this idea, we conducted experiments using genetically-encoded GFP- μ NS
247 particles expressed in *E. coli* and *C. crescentus*. We previously showed that GFP- μ NS particles are

248 useful to probe the biophysical properties of the bacterial cytoplasm (Parry et al., 2014). These
249 probes derive from a mammalian reovirus protein that assembles into spherical objects
250 (Broering et al., 2005; Broering et al., 2002). Once fused to GFP, they form fluorescent particles
251 that increase in signal intensity and absolute size with increased GFP- μ NS synthesis (Parry et al.,
252 2014). We tracked GFP- μ NS particles from three bins of particles of similar intensity (and,
253 consequently, size) in both *E. coli* and *C. crescentus* growing at a similar rate (Figure 6A and Movie
254 S1-2). Comparison of the ensemble-averaged mean squared displacements (MSDs) for particles
255 belonging to these bins revealed drastic differences in probe dynamics between the two species
256 (Figure 6B). GFP- μ NS particles in *C. crescentus*, independent of their size range, displayed
257 significantly lower mobility than in *E. coli* (Figure 6B). Diffusion measurements of free GFP are
258 similar in these two species (Elowitz et al., 1999; Montero Llopis et al., 2012), indicating that a
259 difference in cytoplasmic viscosity cannot explain these observations. Instead, these observations
260 support the notion that different NC ratios can lead to different biophysical properties of the
261 cytoplasm that affect the mobility of large cytoplasmic objects.

262

263 **Ribosome dynamics differ in bacteria with different NC ratio**

264 What large cytoplasmic components may be impacted by differences in NC ratio? Under the
265 conditions we used, GFP- μ NS particles have reported sizes between 50 and 200 nm (Parry et al.,
266 2014), a similar size range as polysomes (Brandt et al., 2009), which are mRNAs loaded with
267 multiple ribosomes (Miller et al., 1970; Warner et al., 1962). If polysome mobility is impacted by
268 the DNA meshwork and the fraction of cellular space it occupies, it may explain a currently
269 unresolved discrepancy in mRNA localization in the literature. Fluorescence *in situ* hybridization
270 (FISH) microscopy experiments on several mRNAs in *C. crescentus* suggest that these mRNAs
271 remain close to their corresponding gene loci throughout most of their lifetime (Montero Llopis
272 et al., 2010). In contrast, a genome-wide FISH study in *E. coli* reveals no spatial enrichment of
273 mRNAs near the corresponding chromosomal regions (Moffitt et al., 2016). Because translation
274 starts on nascent mRNAs, polysomes are expected to form within the nucleoid. However, in *E. coli*,
275 the low NC ratio creates DNA-free regions in which polysomes can more freely diffuse once they
276 escape the DNA meshwork, leading to their dispersion. Conversely, the high NC ratio of *C.*
277 *crescentus* would prevent the escape of polysomes from the DNA meshwork.

278

279 To test this hypothesis, we used photoactivated localization microscopy to track ribosomes in
280 both *E. coli* and *C. crescentus*. In *E. coli*, we labeled ribosomes using a fusion of ribosomal subunit
281 protein S22 with mEos2 (Wang et al., 2011). In *C. crescentus*, we tracked L1-Dendra2-tagged
282 ribosomes (Lim et al., 2014). In both cases, the fusion replaced the wild-type copy of the
283 ribosomal gene at its native chromosomal locus (Lim et al., 2014; Wang et al., 2011). Importantly,

284 we acquired data at five different frame intervals (between 5 and 100 ms) and constructed
285 ensemble MSDs for each frame interval (> 8900 trajectories per frame interval, Figure 6C and
286 Movie S3-4). We reasoned that polysomes diffusing in a DNA meshwork may experience caging
287 and uncaging behaviors, as observed for probes diffusing in gels (Brangwynne et al., 2009; Cai et
288 al., 2011; Guo et al., 2014; Wong et al., 2004). Tracking at multiple timescales may reveal such
289 non-linear dynamics in MSDs. As the majority of ribosomes (~75-80%) are engaged in translation
290 in both organisms (Forchhammer and Lindahl, 1971; Lin et al., 2004; Montero Llopis et al., 2012;
291 Phillips et al., 1969; Varricchio and Monier, 1971), most of our trajectories likely reflected
292 polysome dynamics.

293
294 The MSDs indeed revealed non-linear dynamics, with polysomes in *C. crescentus* displaying lower
295 mobility than those in *E. coli*, especially at the longer (subsecond) timescales (Figure 6C). The
296 difference in MSDs was not due to polysomes “experiencing” cell membrane confinement sooner
297 in *C. crescentus* because of its smaller size than *E. coli*, as higher MSD values were obtained in both
298 organisms following treatment with the transcription initiation inhibitor rifampicin (Figure 6D).
299 Rifampicin treatment results in mRNA depletion, thus converting all polysomes into smaller, and
300 therefore faster, free ribosomes (Blundell and Wild, 1971) that explore more cellular space in the
301 same amount of time (Figure 6D). This finding demonstrates that at the subsecond timescale, cell
302 size does not limit polysome mobility in either organism, and that cell confinement is not
303 responsible for the observed mobility difference between the two species.

304
305 The non-linear dynamics of ribosomes became particularly apparent when we calculated the
306 apparent diffusion coefficient (D_a) and the anomalous exponents (α) from the MSDs. The value
307 for D_a is commonly extracted from the slope of the first few time lags of the MSD curve using the
308 equation $MSD = 4D_a t$ (Michalet, 2010). Anomalous exponents were obtained from the slope of the
309 first three points of the MSD vs. time (as anomalous diffusion in the cytoplasm is characterized
310 by a power law scaling: $MSD(t) \propto t^\alpha$ (Bouchaud and Georges, 1990)). Generally, in biological
311 studies, D_a and α are assumed to be constant over time, such that most single-molecule tracking
312 experiments are done using only a single time frame. However, our analysis revealed a striking
313 dependency of D_a and α on the timescales at which the measurements were made (Figure 6E-F).
314 In both organisms, D_a decreased with longer timescales, while α increased. Furthermore, the
315 difference in D_a between *E. coli* and *C. crescentus* increased with increasing time intervals (Figure
316 6E), and the α value was consistently lower for ribosomes in *C. crescentus* than in *E. coli* (Figure
317 6F). These differences indicate that ribosomes, the majority of which is contained within
318 polysomes, are much more confined in the high NC ratio bacterium *C. crescentus* than in the low
319 NC ratio bacterium *E. coli*.

320

321 In single-molecule tracking experiments, the frame rate is usually under 100 ms to ensure
322 accurate localization determination. However, the lifetime of most bacterial mRNAs is on the
323 minute timescale (Chen et al., 2015; Kristoffersen et al., 2012; Moffitt et al., 2016; Redon et al.,
324 2005). Given the time-dependency of ribosome dynamics, we anticipated that the difference in
325 spatial exploration of ribosomes between *E. coli* and *C. crescentus* would be even more apparent
326 at the physiologically relevant timescale of minutes. This is indeed what we observed in
327 fluorescence recovery after photobleaching (FRAP) microscopy experiments (Figure 6G). To
328 minimize the effects of cell geometry and photobleaching location on the observed fluorescence
329 recovery, we used filamentous cells that were unable to divide due to cephalixin treatment (*E.*
330 *coli*) or FtsZ depletion (*C. crescentus*), as routinely done (Elowitz et al., 1999; Montero Llopis et
331 al., 2012). In these filamentous cells, the NC ratio remained the same as in normal sized cells
332 (Figure S3D and S5D-E). Ribosomes were labeled using a RplA-GFP fusion in both species. RplA
333 is the 50S ribosomal subunit protein L1, previously used to examine ribosome localization in *B.*
334 *subtilis* (Mascarenhas et al., 2001). Due to the heterogenous distribution of the ribosomal signal
335 in *E. coli*, we were unable to quantify ribosome mobility with a simple one or two-state diffusion
336 model, but we did observe clear qualitative differences in ribosomal recovery between the two
337 species (Figure 6G, Movie S5-6). *E. coli* cells showed nearly complete fluorescence recovery at the
338 photobleaching location after 450 s while *C. crescentus* cells often recovered less than 20% of
339 their prebleached fluorescence intensity.

340

341 **Intracellular organization of translation is associated with the NC ratio and cell size**

342 The decreased mobility of polysomes in *C. crescentus* is consistent with the notion that the cell-
343 filling nucleoid impedes polysome motion in this species. In *E. coli*, on the other hand, polysomes
344 display higher mobility likely because they can diffuse more freely and accumulate in DNA-free
345 regions once they escape the DNA meshwork. This raises the intriguing possibility that the
346 difference in NC ratio and its impact on ribosome mobility contribute to the striking difference in
347 spatial organization of ribosomes and thus translation between these two organisms. In *E. coli*, as
348 in other bacteria with low NC ratios like *B. subtilis* and *Lactococcus lactis*, ribosomes are enriched
349 in the nucleoid-free regions of the cytoplasm (Azam et al., 2000; Bakshi et al., 2012; Lewis et al.,
350 2000; Robinow and Kellenberger, 1994; van Gijtenbeek et al., 2016), resulting in partial
351 segregation of transcription and translation. In *C. crescentus* and *Sinorhizobium meliloti*, two
352 bacteria with high NC ratios, a large physical separation of ribosomes and DNA is not observed,
353 as both are found throughout the cytoplasm (Bayas et al., 2018; Montero Llopis et al., 2010).

354

355 If the NC ratio does indeed affect the spatial organization of translation, we may expect to already
356 see changes in ribosome localization in *E. coli* cells grown in different nutritional environments
357 that lead to small variations in NC ratios (Figure 1C, inset). To test this expectation, we used an *E.*
358 *coli* strain carrying a mEos2 fusion to a ribosomal protein (Sanamrad et al., 2014) and grew this
359 strain under 12 growth conditions that result in slightly varying NC ratios. Although nucleoid
360 exclusion of ribosomes was observed for each growth condition, the exclusion was more
361 pronounced in cells with smaller average NC ratios. This is exemplified in Figure 7A showing a
362 comparison between cells in a nutrient-rich medium (M9gluCAAT, average NC ratio = 0.53) and
363 cells in nutrient-poor medium (M9gly, average NC ratio = 0.58). We quantified the average
364 nucleoid exclusion of ribosomes by calculating the signal correlation factor (SCF), a metric that
365 measures the correlation between two fluorescent signals (see STARS Method). An SCF of 1, 0 and
366 -1 indicates that the two signals display perfect co-localization, independent localization and
367 exclusion, respectively. We restricted the calculation of SCF to a specific “correlation area” within
368 individual cells (Figure S8A) to minimize the effects of cell size and geometry on the correlation
369 (see STAR methods). This quantification across 12 growth media with varying NC ratios
370 confirmed the gradual increase in ribosome exclusion with decreasing NC ratio (increasing
371 average cell size), as evidenced by the more negative average SCF values (Figure 7B).

372
373 Given the continuum of NC ratios among diverse species (Figure 4B), we may also expect to see
374 differences in ribosome localization among species with varying NC ratios. To examine this
375 possibility, we performed fluorescence *in situ* hybridization (FISH) microscopy on 10 different
376 species using a Cy5-labeled EUB338 probe complementary to the 5' domain of 16S rRNA (Amann
377 et al., 1990). This probe is complementary to the majority of eubacterial species sequenced and
378 provides a method to visualize bulk ribosome localization in diverse species. As a control, we first
379 performed SCF quantification for an *E. coli* strain producing fluorescently labeled ribosomes. This
380 test revealed that cell fixation, a necessary step of the FISH procedure, slightly affects ribosome
381 and DNA localization, thereby artificially increasing the SCF value (Figure S8B). Despite this
382 caveat, we still observed nucleoid exclusion of ribosomes and strong colocalization between the
383 ribosome signals obtained from the fluorescent labeling (using RlpA-GFP) and the FISH
384 procedure (using Cy5-EUB338) at the single-cell and population levels (Figure 7D-E), validating
385 our FISH method. For the 10 species tested, we found that the SCF obtained by FISH correlates
386 with their average NC ratio (Figure 7F). Given the spectrum of NC ratios among diverse species
387 (Figure 4B) and the correlation between the average NC ratio and the average cell size (Figure 5),
388 our results also suggest a relationship between nucleoid exclusion of ribosomes and average cell
389 size. Indeed, we found a strong negative correlation ($\tau = -0.82$) between the average SCF and the
390 average cell size across the tested species (Figure 7G). In other words, the bigger the average size

391 of the species, the smaller its average NC ratio and the more ribosomes were excluded from the
392 nucleoid. Altogether, our findings suggest a continuum of ribosome organization across bacteria
393 and identify the average NC ratio and cell size of a species in a given growth medium as good
394 predictors of how this bacterium spatially organizes translation.

395

396 **Discussion**

397 Although the first reports of scaling relationships in eukaryotes between the size of subcellular
398 components and that of the cell date back more than 100 years (Conklin, 1912; Marshall, 2015;
399 Wilson, 1925; Woodruff, 1913), this phenomenon has remained largely unexplored in bacteria.
400 Here, we demonstrate that nucleoid size strongly scales with cell size in exponentially growing
401 cultures across a wide range of cell sizes and a diverse panel of bacterial species (Figures 1, 2, 3,
402 4, S1, S3D, S4, S5 and S6). Despite the apparently conserved nature of nucleoid size scaling, we
403 found a continuum of NC ratios across species (Figure 4B), which can be predicted from the
404 average cell size of the bacterial population (Figure 5). We highlight important biological
405 implications of having a different NC ratio for the mobility and localization of larger particles such
406 as polysomes (Figure 6), thereby implicating the NC ratio as an important determinant of the
407 intracellular organization of bacterial translation (Figure 7).

408

409 Using the model bacteria *E. coli* and *C. crescentus*, we show that the scaling of nucleoid size with
410 cell size occurs in the absence of changes in DNA content (Figure 2B-D and 3B). This is in line with
411 findings in yeast cells in which increases in the amount of DNA do not directly lead to increases
412 in nuclear size (Jorgensen et al., 2007; Neumann and Nurse, 2007). In eukaryotes, nuclear
413 structural components, nucleocytoplasmic transport and nuclear envelope expansion have all
414 been implicated in regulating nuclear size (Hara and Merten, 2015; Jevtic et al., 2014; Kume et al.,
415 2017; Levy and Heald, 2010). The fact that the scaling property extends to bacteria, which lack a
416 nuclear envelope, makes it even more remarkable. It highlights an intrinsic property of the DNA
417 and the cell that predates the development of membrane-enclosed organelles such as the nucleus.
418 The fact that it arises regardless of the way the genome is packaged into the cell (independently
419 of nuclear membrane or histones) suggests that it is an ancient and basic cellular feature.

420

421 Although nucleoid size scaling is widespread among bacteria, the resulting NC ratios vary
422 considerably (Figure 4B). Here again, this is similar to what is observed in eukaryotes where the
423 NC ratio varies greatly among cell types (Ganguly et al., 2016; Jevtic and Levy, 2015; Jorgensen et
424 al., 2007; Kume et al., 2017; Neumann and Nurse, 2007; Novakova et al., 2016; Su Lim et al., 2015).
425 We found no link between NC ratio and chromosome size or growth rate of a given species (Figure
426 S6). Instead, we discovered a remarkable relationship between the average cell size of a

427 population and its average NC ratio, as the latter strongly correlated with morphological metrics
428 that reflect average cell size (i.e., average cell volume, length, width, area and surface area to
429 volume ratio) (Figure 5). Although the relationship is strongest for the average cell volume, the
430 strong correlations with other size-related variables currently preclude us from associating the
431 NC ratio with a specific morphological feature. It is important to note that while the relationship
432 between average cell size and average NC ratio has predictive value at the population level, it does
433 not extend to the single-cell level. This is evident from the maintenance of the NC ratio over the
434 course of a cell cycle (Figure 1) and is further exemplified by the fact that an overlap in cell size
435 between *C. crescentus* and *E. coli* does not lead to an overlap in NC ratio at the single-cell level
436 (Figure 3C). These findings indicate that although a general relationship between average cell size
437 and the NC ratio exists, the latter is controlled by factors other than cell size at the single-cell level.
438

439 Differences in NC ratio among species and across growth conditions (Figures 1C and 4B) have
440 physiological implications. By comparing the motion of ribosomes in *E. coli* and *C. crescentus*, we
441 found that their mobility is significantly decreased in cells with high NC ratios. Given that
442 cytoplasmic viscosity is similar in *E. coli* and *C. crescentus* based on GFP diffusion measurements
443 (Elowitz et al., 1999; Montero Llopis et al., 2012), this reduction likely arises because the diffusion
444 of polysomes is impeded by the DNA meshwork. This difference was most pronounced on longer
445 timescales due to the time-dependent properties of ribosome movement (both in terms of D_a and
446 α). These non-linear dynamics of polysomes inside the bacterial cytoplasm reveal that the DNA
447 affects the biophysical properties of the bacterial cytoplasm. Our data suggest that polysomes and
448 other similarly sized objects experience local caging when they encounter the DNA mesh. An
449 implication of such non-linear dynamics is that direct comparisons of diffusion coefficients
450 without considering physiologically relevant timescales and differences in α can be misleading.
451 For example, at short frame rates, polysomes may not diffuse far enough to be “aware” that they
452 are within a DNA meshwork. As a result, the D_a values in *E. coli* and *C. crescentus* are relatively
453 close to each other, consistent with previous determinations (Bakshi et al., 2012; Bayas et al.,
454 2018; Sanamrad et al., 2014). This could lead to the interpretation that ribosome dynamics are
455 the same in these organisms. We show that this is true only at the millisecond timescale, a
456 timescale at which polysomes primarily experience protein crowding, which is similar in the two
457 species (Elowitz et al., 1999; Montero Llopis et al., 2012). As the timescale increases, the D_a values
458 decrease as polysomes increasingly experience the DNA mesh. This highlights the non-linear
459 biophysical properties of the bacterial cytoplasm and stresses the importance of making diffusion
460 measurements at different length and time scales.

461

462 The decrease in D_a values over time is most dramatic in *C. crescentus* (Figure 5E) where, unlike in
463 *E. coli*, polysomes cannot escape the DNA meshwork because it fills most of the cell. By
464 themselves, the differences in ribosome mobility in *E. coli* and *C. crescentus* could be attributed to
465 other factors (e.g., fraction of nascent vs. mature mRNAs) than a difference in NC ratio between
466 the two species. However, the decreased mobility of genetically encoded GFP- μ NS particles in *C.*
467 *crescentus* (in comparison to *E. coli*) supports our interpretation that different NC ratios give rise
468 to different physical properties of the cytoplasm and have widespread implications for larger
469 cellular components and their associated processes. The reduction of polysome mobility in *C.*
470 *crescentus* explains why mRNAs remain in close proximity to their corresponding gene loci in this
471 organism (Montero Llopis et al., 2010). In *E. coli*, on the other hand, polysomes would be able to
472 escape the nucleoid due to the lower NC ratio, after which their increased mobility would lead to
473 a more dispersed mRNA localization, as recently shown (Moffitt et al., 2016). Based on this
474 interpretation, we anticipate that the NC ratio of a given bacterium, together with the lifetime of
475 the mRNA, will dictate whether protein synthesis from this mRNA primarily occurs near the gene
476 locus where the mRNA was transcribed, or away from it.

477

478 In eukaryotes, the term cytosol is used to designate the part of the cytoplasm that is not held by
479 organelles. We propose that a similar distinction can be made in bacteria. Even without a
480 membrane-enforced separation, the nucleoid (organelle) provides a distinct biophysical
481 environment from the DNA-free region of the cytoplasm (cytosol). The spectrum of NC ratios
482 across species and growth conditions suggests that the cytosolic fraction of a bacterial cell is far
483 from fixed, and is instead an evolvable feature (Figure 4B). Although the NC ratio depends on the
484 growth conditions for a given species, the actual fluctuations between conditions are small in
485 comparison to the entire spectrum observed across species (Figures 1C and 5B). This observation
486 may reflect unappreciated evolutionary constraints on intracellular organization and cell size for
487 a given bacterial species.

488

489 **Acknowledgements**

490 We thank Drs. Nora Ausmees, Jacques Batut, Steven Lindow, Savithamma Dinesh-Kumar, Jeanne
491 S. Poindexter, Jo Handelsman, Bonnie Bassler, Peter Greenberg, David Zusman, Wade Winkler,
492 Pamela Brown, Eric Stabb, Mark McBride, Sunny Xie, Andrew Goodman, as well as the ATCC
493 Bacteriology collection and the Yale *E. coli* Genetic Stock Center, for providing strains used in this
494 work. We would specifically like to thank Drs. Andrew Goodman and Bentley Lim for sharing fixed
495 *B. theta* cells harvested from monocolonized mice, and Dr. Michael Zimmerman for providing
496 strains and for his help with setting up anaerobic growth experiments. We also thank the Jacobs-

497 Wagner laboratory for fruitful discussions and for critical reading of the manuscript. This work
498 was partly supported by the National Institutes of Health (R01 GM065835 to C.J.-W.). S.K.G. was
499 partly funded by a fellowship from the Belgian American Education Foundation (B.A.E.F.). C.J.-W.
500 is an investigator of the Howard Hughes Medical Institute.

501

502 **Author contributions**

503 Conceptualization, W.T.G., S.K.G. and C.J.-W.; Methodology, W.T.G., S.K.G., Y.X., B.R.P., M.C. S.K. and
504 C.J.-W. Software, W.T.G., S.K.G., Y.X., B.R.P. and M.C.; Formal Analysis, W.T.G., S.K.G., Y.X. and B.R.P.;
505 Investigation, W.T.G. and S.K.G.; Data Curation, W.T.G., S.K.G., Y.X. and B.R.P.; Writing – Original
506 Draft, S.K.G. and C.J.-W.; Writing – Review & Editing, W.T.G., S.K.G., Y.X., B.R.P., M.C., S.K., and C.J.-
507 W; Visualization, W.T.G. and C.J.-W.; Supervision, C.J.-W.; Project Administration, C.J.-W.; Funding
508 Acquisition, C.J.-W.

509

510 **Declaration of Interests**

511 The authors declare no competing interests.

512

513 **References**

514 Adiciptaningrum, A., Osella, M., Moolman, M.C., Cosentino Lagomarsino, M., and Tans, S.J. (2015).
515 Stochasticity and homeostasis in the *E. coli* replication and division cycle. *Sci Rep* 5, 18261.

516

517 Alyahya, S.A., Alexander, R., Costa, T., Henriques, A.O., Emonet, T., and Jacobs-Wagner, C. (2009).
518 RodZ, a component of the bacterial core morphogenic apparatus. *Proc Natl Acad Sci U S A* 106,
519 1239-1244.

520

521 Amann, R.I., Binder, B.J., Olson, R.J., Chisholm, S.W., Devereux, R., and Stahl, D.A. (1990).
522 Combination of 16S rRNA-targeted oligonucleotide probes with flow cytometry for analyzing
523 mixed microbial populations. *Appl Environ Microbiol* 56, 1919-1925.

524

525 Arias-Cartin, R., Dobihal, G.S., Campos, M., Surovtsev, I.V., Parry, B., and Jacobs-Wagner, C. (2017).
526 Replication fork passage drives asymmetric dynamics of a critical nucleoid-associated protein in
527 *Caulobacter*. *EMBO J* 36, 301-318.

528

529 Azam, T.A., Hiraga, S., and Ishihama, A. (2000). Two types of localization of the DNA-binding
530 proteins within the *Escherichia coli* nucleoid. *Genes Cells* 5, 613-626.

531

532 Bacic, M.K., and Smith, C.J. (2008). Laboratory maintenance and cultivation of *Bacteroides* species.
533 *Curr Protoc Microbiol Chapter 13*, Unit 13C 11.

534

535 Bakshi, S., Siryaporn, A., Goulian, M., and Weisshaar, J.C. (2012). Superresolution imaging of
536 ribosomes and RNA polymerase in live *Escherichia coli* cells. *Mol Microbiol* 85, 21-38.

537

538 Bayas, C.A., Wang, J., Lee, M.K., Schrader, J.M., Shapiro, L., and Moerner, W.E. (2018). Spatial
539 organization and dynamics of RNase E and ribosomes in *Caulobacter crescentus*. *Proc Natl Acad Sci U S A* 115, E3712-E3721.

540

541
542 Bisson-Filho, A.W., Zheng, J., and Garner, E. (2018). Archaeal imaging: leading the hunt for new
543 discoveries. *Mol Biol Cell* 29, 1675-1681.
544
545 Blundell, M.R., and Wild, D.G. (1971). Altered ribosomes after inhibition of *Escherichia coli* by
546 rifampicin. *Biochem J* 121, 391-398.
547
548 Bouchaud, J.P., and Georges, A. (1990). Anomalous diffusion in disordered media - Statistical
549 mechanisms, models and physical applications. *Phys Rep* 195, 127-293.
550
551 Bowman, G.R., Comolli, L.R., Zhu, J., Eckart, M., Koenig, M., Downing, K.H., Moerner, W.E., Earnest,
552 T., and Shapiro, L. (2008). A polymeric protein anchors the chromosomal origin/ParB complex at
553 a bacterial cell pole. *Cell* 134, 945-955.
554
555 Boye, E., and Lobner-Olesen, A. (1991). Bacterial growth control studied by flow cytometry. *Res*
556 *Microbiol* 142, 131-135.
557
558 Brandt, F., Etchells, S.A., Ortiz, J.O., Elcock, A.H., Hartl, F.U., and Baumeister, W. (2009). The native
559 3D organization of bacterial polysomes. *Cell* 136, 261-271.
560
561 Brangwynne, C.P., Koenderink, G.H., MacKintosh, F.C., and Weitz, D.A. (2009). Intracellular
562 transport by active diffusion. *Trends Cell Biol* 19, 423-427.
563
564 Brendler, T., Abeles, A., and Austin, S. (1995). A protein that binds to the P1 origin core and the
565 oriC 13mer region in a methylation-specific fashion is the product of the host *seqA* gene. *EMBO J*
566 14, 4083-4089.
567
568 Broering, T.J., Arnold, M.M., Miller, C.L., Hurt, J.A., Joyce, P.L., and Nibert, M.L. (2005). Carboxyl-
569 proximal regions of reovirus nonstructural protein muNS necessary and sufficient for forming
570 factory-like inclusions. *J Virol* 79, 6194-6206.
571
572 Broering, T.J., Parker, J.S., Joyce, P.L., Kim, J., and Nibert, M.L. (2002). Mammalian reovirus
573 nonstructural protein microNS forms large inclusions and colocalizes with reovirus microtubule-
574 associated protein micro2 in transfected cells. *J Virol* 76, 8285-8297.
575
576 Cagliero, C., and Jin, D.J. (2013). Dissociation and re-association of RNA polymerase with DNA
577 during osmotic stress response in *Escherichia coli*. *Nucleic Acids Res* 41, 315-326.
578
579 Cai, L.H., Panyukov, S., and Rubinstein, M. (2011). Mobility of Nonsticky Nanoparticles in Polymer
580 Liquids. *Macromolecules* 44, 7853-7863.
581
582 Campos, M., Govers, S.K., Irnov, I., Dobihal, G.S., Cornet, F., and Jacobs-Wagner, C. (2018).
583 Genomewide phenotypic analysis of growth, cell morphogenesis, and cell cycle events in
584 *Escherichia coli*. *Mol Syst Biol* 14, e7573.
585
586 Campos, M., and Jacobs-Wagner, C. (2013). Cellular organization of the transfer of genetic
587 information. *Curr Opin Microbiol* 16, 171-176.
588
589 Capell, B.C., and Collins, F.S. (2006). Human laminopathies: nuclei gone genetically awry. *Nat Rev*
590 *Genet* 7, 940-952.
591
592 Carl, P.L. (1970). *Escherichia coli* mutants with temperature-sensitive synthesis of DNA. *Mol Gen*
593 *Genet* 109, 107-122.
594

- 595 Chen, H., Shiroguchi, K., Ge, H., and Xie, X.S. (2015). Genome-wide study of mRNA degradation and
596 transcript elongation in *Escherichia coli*. *Mol Syst Biol* *11*, 781.
597
- 598 Chow, K.H., Factor, R.E., and Ullman, K.S. (2012). The nuclear envelope environment and its cancer
599 connections. *Nat Rev Cancer* *12*, 196-209.
600
- 601 Collier, J., and Shapiro, L. (2009). Feedback control of DnaA-mediated replication initiation by
602 replisome-associated HdaA protein in *Caulobacter*. *J Bacteriol* *191*, 5706-5716.
603
- 604 Conklin, E.G. (1912). Cell size and nuclear size. *J Exp Zool* *12*, 1-98.
605
- 606 Cooper, S., and Helmstetter, C.E. (1968). Chromosome replication and the division cycle of
607 *Escherichia coli* B/r. *J Mol Biol* *31*, 519-540.
608
- 609 Crocker, J.C., and Grier, D.G. (1996). Methods of digital video microscopy for colloidal studies. *J*
610 *Colloid Interf Sci* *179*, 298-310.
611
- 612 Diekmann, Y., and Pereira-Leal, J.B. (2013). Evolution of intracellular compartmentalization.
613 *Biochem J* *449*, 319-331.
614
- 615 Ebersbach, G., Briegel, A., Jensen, G.J., and Jacobs-Wagner, C. (2008). A self-associating protein
616 critical for chromosome attachment, division, and polar organization in *Caulobacter*. *Cell* *134*,
617 956-968.
618
- 619 Eley, A., Greenwood, D., and O'Grady, F. (1985). Comparative growth of *Bacteroides* species in
620 various anaerobic culture media. *J Med Microbiol* *19*, 195-201.
621
- 622 Elowitz, M.B., Surette, M.G., Wolf, P.E., Stock, J.B., and Leibler, S. (1999). Protein mobility in the
623 cytoplasm of *Escherichia coli*. *J Bacteriol* *181*, 197-203.
624
- 625 Fernandez-Fernandez, C., Grosse, K., Sourjik, V., and Collier, J. (2013). The beta-sliding clamp
626 directs the localization of HdaA to the replisome in *Caulobacter crescentus*. *Microbiology* *159*,
627 2237-2248.
628
- 629 Forchhammer, J., and Lindahl, L. (1971). Growth rate of polypeptide chains as a function of the
630 cell growth rate in a mutant of *Escherichia coli* 15. *J Mol Biol* *55*, 563-568.
631
- 632 Ganguly, A., Bhattacharjee, C., Bhave, M., Kailaje, V., Jain, B.K., Sengupta, I., Rangarajan, A., and
633 Bhattacharyya, D. (2016). Perturbation of nucleo-cytoplasmic transport affects size of nucleus
634 and nucleolus in human cells. *FEBS Lett* *590*, 631-643.
635
- 636 Goodman, A.L., Kallstrom, G., Faith, J.J., Reyes, A., Moore, A., Dantas, G., and Gordon, J.I. (2011).
637 Extensive personal human gut microbiota culture collections characterized and manipulated in
638 gnotobiotic mice. *Proc Natl Acad Sci U S A* *108*, 6252-6257.
639
- 640 Guo, M., Ehrlicher, A.J., Jensen, M.H., Renz, M., Moore, J.R., Goldman, R.D., Lippincott-Schwartz, J.,
641 Mackintosh, F.C., and Weitz, D.A. (2014). Probing the stochastic, motor-driven properties of the
642 cytoplasm using force spectrum microscopy. *Cell* *158*, 822-832.
643
- 644 Hara, Y., and Merten, C.A. (2015). Dynein-based accumulation of membranes regulates nuclear
645 expansion in *Xenopus laevis* egg extracts. *Dev Cell* *33*, 562-575.
646
- 647 Harold, F.M. (2005). Molecules into cells: specifying spatial architecture. *Microbiol Mol Biol Rev*
648 *69*, 544-564.

649
650 Helgesen, E., Fossum-Raunehaug, S., Saetre, F., Schink, K.O., and Skarstad, K. (2015). Dynamic
651 *Escherichia coli* SeqA complexes organize the newly replicated DNA at a considerable distance
652 from the replisome. *Nucleic Acids Res* 43, 2730-2743.
653
654 Irnov, I., Wang, Z., Jannetty, N.D., Bustamante, J.A., Rhee, K.Y., and Jacobs-Wagner, C. (2017).
655 Crosstalk between the tricarboxylic acid cycle and peptidoglycan synthesis in *Caulobacter*
656 *crenscentus* through the homeostatic control of alpha-ketoglutarate. *PLoS Genet* 13, e1006978.
657
658 Jaqaman, K., Loerke, D., Mettlen, M., Kuwata, H., Grinstein, S., Schmid, S.L., and Danuser, G. (2008).
659 Robust single-particle tracking in live-cell time-lapse sequences. *Nat Methods* 5, 695-702.
660
661 Jensen, R.B., and Shapiro, L. (1999). The *Caulobacter crescentus smc* gene is required for cell cycle
662 progression and chromosome segregation. *Proc Natl Acad Sci U S A* 96, 10661-10666.
663
664 Jevtic, P., Edens, L.J., Vukovic, L.D., and Levy, D.L. (2014). Sizing and shaping the nucleus:
665 mechanisms and significance. *Curr Opin Cell Biol* 28, 16-27.
666
667 Jevtic, P., and Levy, D.L. (2015). Nuclear size scaling during *Xenopus* early development
668 contributes to midblastula transition timing. *Curr Biol* 25, 45-52.
669
670 Jorgensen, P., Edgington, N.P., Schneider, B.L., Rupes, I., Tyers, M., and Futcher, B. (2007). The size
671 of the nucleus increases as yeast cells grow. *Mol Biol Cell* 18, 3523-3532.
672
673 Junier, I., Boccard, F., and Espeli, O. (2014). Polymer modeling of the *E. coli* genome reveals the
674 involvement of locus positioning and macrodomain structuring for the control of chromosome
675 conformation and segregation. *Nucleic Acids Res* 42, 1461-1473.
676
677 Kellenberger, E., Ryter, A., and Sechaud, J. (1958). Electron microscope study of DNA-containing
678 plasmids. II. Vegetative and mature phage DNA as compared with normal bacterial nucleoids in
679 different physiological states. *J Biophys Biochem Cytol* 4, 671-678.
680 Kim, S., and Jacobs-Wagner, C. (2018). Effects of mRNA degradation and site-specific
681 transcriptional pausing on protein expression noise. *Biophys J* 114, 1718-1729.
682
683 Kristoffersen, S.M., Haase, C., Weil, M.R., Passalacqua, K.D., Niazi, F., Hutchison, S.K., Desany, B.,
684 Kolsto, A.B., Tourasse, N.J., Read, T.D., *et al.* (2012). Global mRNA decay analysis at single
685 nucleotide resolution reveals segmental and positional degradation patterns in a Gram-positive
686 bacterium. *Genome Biol* 13, R30.
687
688 Kume, K., Cantwell, H., Neumann, F.R., Jones, A.W., Snijders, A.P., and Nurse, P. (2017). A
689 systematic genomic screen implicates nucleocytoplasmic transport and membrane growth in
690 nuclear size control. *PLoS Genet* 13, e1006767.
691
692 Levy, D.L., and Heald, R. (2010). Nuclear size is regulated by importin alpha and Ntf2 in *Xenopus*.
693 *Cell* 143, 288-298.
694
695 Levy, D.L., and Heald, R. (2012). Mechanisms of intracellular scaling. *Annu Rev Cell Dev Biol* 28,
696 113-135.
697
698 Lewis, P.J., Thaker, S.D., and Errington, J. (2000). Compartmentalization of transcription and
699 translation in *Bacillus subtilis*. *EMBO J* 19, 710-718.
700

- 701 Lim, H.C., Surovtsev, I.V., Beltran, B.G., Huang, F., Bewersdorf, J., and Jacobs-Wagner, C. (2014).
702 Evidence for a DNA-relay mechanism in ParABS-mediated chromosome segregation. *Elife* 3,
703 e02758.
704
- 705 Lin, B., Thayer, D.A., and Maddock, J.R. (2004). The *Caulobacter crescentus* CgtAC protein
706 cosediments with the free 50S ribosomal subunit. *J Bacteriol* 186, 481-489.
707
- 708 Lu, M., Campbell, J.L., Boye, E., and Kleckner, N. (1994). SeqA: a negative modulator of replication
709 initiation in *E. coli*. *Cell* 77, 413-426.
710
- 711 Marshall, W.F. (2015). Subcellular size. *Cold Spring Harb Perspect Biol* 7.
712
- 713 Mascarenhas, J., Weber, M.H., and Graumann, P.L. (2001). Specific polar localization of ribosomes
714 in *Bacillus subtilis* depends on active transcription. *EMBO Rep* 2, 685-689.
715
- 716 Mason, D.J., and Powelson, D.M. (1956). Nuclear division as observed in live bacteria by a new
717 technique. *J Bacteriol* 71, 474-479.
718
- 719 Michalet, X. (2010). Mean square displacement analysis of single-particle trajectories with
720 localization error: Brownian motion in an isotropic medium. *Phys Rev E Stat Nonlin Soft Matter*
721 *Phys* 82, 041914.
722
- 723 Miller, O.L., Jr., Hamkalo, B.A., and Thomas, C.A., Jr. (1970). Visualization of bacterial genes in
724 action. *Science* 169, 392-395.
725
- 726 Moffitt, J.R., Pandey, S., Boettiger, A.N., Wang, S., and Zhuang, X. (2016). Spatial organization
727 shapes the turnover of a bacterial transcriptome. *Elife* 5, e13065.
728
- 729 Molina, F., and Skarstad, K. (2004). Replication fork and SeqA focus distributions in *Escherichia*
730 *coli* suggest a replication hyperstructure dependent on nucleotide metabolism. *Mol Microbiol* 52,
731 1597-1612.
732
- 733 Montero Llopis, P., Jackson, A.F., Sliusarenko, O., Surovtsev, I., Heinritz, J., Emonet, T., and Jacobs-
734 Wagner, C. (2010). Spatial organization of the flow of genetic information in bacteria. *Nature* 466,
735 77-81.
736
- 737 Montero Llopis, P., Sliusarenko, O., Heinritz, J., and Jacobs-Wagner, C. (2012). *In vivo* biochemistry
738 in bacterial cells using FRAP: insight into the translation cycle. *Biophys J* 103, 1848-1859.
739
- 740 Neumann, F.R., and Nurse, P. (2007). Nuclear size control in fission yeast. *J Cell Biol* 179, 593-600.
741
- 742 Novakova, L., Kovacovicova, K., Dang-Nguyen, T.Q., Sodek, M., Skultety, M., and Anger, M. (2016).
743 A balance between nuclear and cytoplasmic volumes controls spindle length. *PloS One* 11,
744 e0149535.
745
- 746 Paintdakhi, A., Parry, B., Campos, M., Irnov, I., Elf, J., Surovtsev, I., and Jacobs-Wagner, C. (2016).
747 Oufiti: an integrated software package for high-accuracy, high-throughput quantitative
748 microscopy analysis. *Mol Microbiol* 99, 767-777.
749
- 750 Parry, B.R., Surovtsev, I.V., Cabeen, M.T., O'Hern, C.S., Dufresne, E.R., and Jacobs-Wagner, C. (2014).
751 The bacterial cytoplasm has glass-like properties and is fluidized by metabolic activity. *Cell* 156,
752 183-194.
753

- 754 Phillips, L.A., Hotham-Iglewski, B., and Franklin, R.M. (1969). Polyribosomes of *Escherichia coli*. II.
755 Experiments to determine the *in vivo* distribution of polysomes, ribosomes and ribosomal
756 subunits. *J Mol Biol* *45*, 23-38.
757
- 758 Pierucci, O. (1978). Dimensions of *Escherichia coli* at various growth rates: model for envelope
759 growth. *J Bacteriol* *135*, 559-574.
760
- 761 Prokocimer, M., Davidovich, M., Nissim-Rafinia, M., Wiesel-Motiuk, N., Bar, D.Z., Barkan, R.,
762 Meshorer, E., and Gruenbaum, Y. (2009). Nuclear lamins: key regulators of nuclear structure and
763 activities. *J Cell Mol Med* *13*, 1059-1085.
764
- 765 Reber, S., and Goehring, N.W. (2015). Intracellular Scaling Mechanisms. *Cold Spring Harb Perspect*
766 *Biol* *7*.
767
- 768 Redon, E., Loubiere, P., and Cacaïgn-Bousquet, M. (2005). Role of mRNA stability during genome-
769 wide adaptation of *Lactococcus lactis* to carbon starvation. *J Biol Chem* *280*, 36380-36385.
770
- 771 Robinow, C., and Kellenberger, E. (1994). The bacterial nucleoid revisited. *Microbiol Rev* *58*, 211-
772 232.
773
- 774 Rolinson, G.N. (1980). Effect of beta-lactam antibiotics on bacterial cell growth rate. *J Gen*
775 *Microbiol* *120*, 317-323.
776
- 777 Sanamrad, A., Persson, F., Lundius, E.G., Fange, D., Gynna, A.H., and Elf, J. (2014). Single-particle
778 tracking reveals that free ribosomal subunits are not excluded from the *Escherichia coli* nucleoid.
779 *Proc Natl Acad Sci U S A* *111*, 11413-11418.
780
- 781 Schaechter, M., Maaloe, O., and Kjeldgaard, N.O. (1958). Dependency on medium and temperature
782 of cell size and chemical composition during balanced grown of *Salmonella typhimurium*. *J Gen*
783 *Microbiol* *19*, 592-606.
784
- 785 Shi, H., Colavin, A., Bigos, M., Tropini, C., Monds, R.D., and Huang, K.C. (2017). Deep phenotypic
786 mapping of bacterial cytoskeletal mutants reveals physiological robustness to cell size. *Curr Biol*
787 *27*, 3419-3429 e3414.
788
- 789 Slater, S., Wold, S., Lu, M., Boye, E., Skarstad, K., and Kleckner, N. (1995). *E. coli* SeqA protein binds
790 *oriC* in two different methyl-modulated reactions appropriate to its roles in DNA replication
791 initiation and origin sequestration. *Cell* *82*, 927-936.
792
- 793 Su Lim, C., Sun Kim, E., Yeon Kim, J., Taek Hong, S., Jai Chun, H., Eun Kang, D., and Rae Cho, B.
794 (2015). Measurement of the nucleus area and nucleus/cytoplasm and mitochondria/nucleus
795 ratios in human colon tissues by dual-colour two-photon microscopy imaging. *Sci Rep* *5*, 18521.
796
- 797 Sun, H., Yang, Z., and Shi, W. (1999). Effect of cellular filamentation on adventurous and social
798 gliding motility of *Myxococcus xanthus*. *Proc Natl Acad Sci U S A* *96*, 15178-15183.
799
- 800 Surovtsev, I.V., and Jacobs-Wagner, C. (2018). Subcellular organization: a critical feature of
801 bacterial cell replication. *Cell* *172*, 1271-1293.
802
- 803 Taheri-Araghi, S., Bradde, S., Sauls, J.T., Hill, N.S., Levin, P.A., Paulsson, J., Vergassola, M., and Jun,
804 S. (2015). Cell-size control and homeostasis in bacteria. *Curr Biol* *25*, 385-391.
805

- 806 van Gijtenbeek, L.A., Robinson, A., van Oijen, A.M., Poolman, B., and Kok, J. (2016). On the Spatial
807 Organization of mRNA, Plasmids, and Ribosomes in a Bacterial Host Overexpressing Membrane
808 Proteins. *PLoS Genet* 12, e1006523.
809
- 810 Varricchio, F., and Monier, R. (1971). Ribosome patterns in *Escherichia coli* growing at various
811 rates. *J Bacteriol* 108, 105-110.
812
- 813 Wallden, M., Fange, D., Lundius, E.G., Baltekin, O., and Elf, J. (2016). The synchronization of
814 replication and division cycles in individual *E. coli* cells. *Cell* 166, 729-739.
815
- 816 Wang, W., Li, G.W., Chen, C., Xie, X.S., and Zhuang, X. (2011). Chromosome organization by a
817 nucleoid-associated protein in live bacteria. *Science* 333, 1445-1449.
818
- 819 Wang, Y., Jones, B.D., and Brun, Y.V. (2001). A set of *ftsZ* mutants blocked at different stages of cell
820 division in *Caulobacter*. *Mol Microbiol* 40, 347-360.
821 Warner, J.R., Rich, A., and Hall, C.E. (1962). Electron microscope studies of ribosomal clusters
822 synthesizing hemoglobin. *Science* 138, 1399-1403.
823
- 824 Weart, R.B., Lee, A.H., Chien, A.C., Haeusser, D.P., Hill, N.S., and Levin, P.A. (2007). A metabolic
825 sensor governing cell size in bacteria. *Cell* 130, 335-347.
826
- 827 Wilson, E.B. (1925). Thekaryoplasmic ratio. In the cell in development and heredity (New York:
828 The Macmillan Company), pp. 727-733.
829
- 830 Wong, I.Y., Gardel, M.L., Reichman, D.R., Weeks, E.R., Valentine, M.T., Bausch, A.R., and Weitz, D.A.
831 (2004). Anomalous diffusion probes microstructure dynamics of entangled F-actin networks.
832 *Phys Rev Lett* 92, 178101.
833
- 834 Woodruff, L.L. (1913). Cell size, nuclear size and the nucleo-cytoplasmic relation during the life
835 of a pedigreed race of *oxytricha fallax*. *J Exp Zool* 15, 1-22.
836
- 837 Zink, D., Fischer, A.H., and Nickerson, J.A. (2004). Nuclear structure in cancer cells. *Nat Rev Cancer*
838 4, 677-687.
839
- 840 Zwietering, M.H., Jongenburger, I., Rombouts, F.M., and van 't Riet, K. (1990). Modeling of the
841 bacterial growth curve. *Appl Environ Microbiol* 56, 1875-1881.
842
843

844 **Figure legends**

845 **Figure 1. Nucleoid size scaling is robust across a wide range of *E. coli* cell sizes.**

846 A. Phase contrast and DAPI images of *E. coli* cells (CJW6324) grown in liquid cultures of M9
847 medium supplemented with 0.2% mannose (M9mann) or 0.2% glucose, 0.1% casamino acids and
848 1µg/ml thiamine (M9gluCAAT) at 37 °C. The images were processed with Oufiti to identify the
849 contours of the cells (green) and nucleoids (purple, insets).

850 B. Density contour plots showing the strong correlation between cell area and nucleoid area for
851 individual CJW6324 cells grown in the indicated growth media (for a full description of the
852 growth media, see Table S1). The contour lines represent the 0.10, 0.25, 0.50 and 0.75 probability
853 envelopes of the data.

854 C. Scatter plot of the average cell area versus the average nucleoid area for the indicated growth
855 conditions. Inset: scatter plot of the average cell area versus the average NC ratio for the same
856 growth conditions. Error bars indicate 95% confidence intervals.

857 See also Figures S1-3.

858

859 **Figure 2. Nucleoid size scaling with cell size does not depend on DNA replication.**

860 A. Density scatter plot (left) and density contour plot (right) of cell area versus the relative SeqA-
861 mCherry signal area of *E. coli* cells (CJW6324) grown in M9 medium supplemented with 0.2%
862 glycerol. The gray scale in the density scatter plot indicates the relative density of dots (cells) in
863 a given area of the chart. This plot was used to identify cells in the B, C and D cell cycle periods
864 found under these growth conditions. The contour lines represent the 0.10, 0.25, 0.50 and 0.75
865 probability envelopes of the data. Insets: representative images of the subcellular SeqA-mCherry
866 signal in a specific cell cycle period.

867 B. Density contour plots of cell area versus nucleoid area for cells in B, C and D periods based on
868 the analysis shown in A. The contour lines represent the 0.10, 0.25, 0.50 and 0.75 probability
869 envelopes of the data. The nucleoid was detected by DAPI staining. See also Figure S4.

870 C. Representative fluorescence images of *dnaC2* cells (CJW6370) producing HU-mCherry at
871 different time points after a shift to a restrictive temperature (37 °C).

872 D. Plot showing the average nucleoid area per cell area bin for HU-mCherry-labeled *dnaC2* cells
873 at 37 °C. Cells (n = 12268) from different time points following temperature shifts were combined
874 into one dataset and grouped into bins based on their cell areas. Shown are the average nucleoid
875 area and standard deviation (SD) of each cell area bin. The solid yellow line indicates the expected
876 relationship between nucleoid and cell area based on the scaling observed under permissive
877 conditions (30 °C). The dotted lines indicate the 99% confidence interval (CI) of the fit.

878

879 **Figure 3. Nucleoid size scaling is also observed in *C. crescentus*, a bacterium with a different
880 NC ratio.**

881 All contour lines represent the 0.10, 0.25, 0.50 and 0.75 probability envelopes of the data.

882 A. Density contour plot of cell area versus the relative DnaN-CFP signal area of *C. crescentus* cells
883 producing a DnaN-CFP fusion (CJW5969) and grown in M2 medium supplemented with 0.2%
884 glucose. This plot was used to identify cells in the B, C, and D cell cycle periods. Insets:
885 representative images of the subcellular DnaN-CFP signal in a specific cell cycle period.

886 B. Density contour plots of cell area versus nucleoid area for cells in panel A. The nucleoid was
887 detected by HU-mCherry labeling.

888 C. Density contour plots of cell area versus NC ratio for *E. coli* (CJW6324) and *C. crescentus*
889 (CJW5969) cells grown in M9 medium supplemented with 0.2% glycerol and M2 medium

890 supplemented with 0.2% glucose, respectively. The nucleoid was detected by DAPI staining for *E.*
891 *coli* and by HU-mCherry labeling for *C. crescentus*.

892 See also Figure S5.

893

894 **Figure 4. Nucleoid size scaling across bacterial species from different phyla reveals a**
895 **continuum of NC ratios.**

896 A. Density contour plots of cell area versus nucleoid area for fixed cell populations from different
897 bacterial species. The contour lines represent the 0.10, 0.25, 0.50 and 0.75 probability envelopes
898 of the data. When different growth conditions were examined for the same species, the growth
899 medium is indicated next to the species name. Contours of the same color indicate affiliation to
900 the same phylum or class. The DNA dye used for nucleoid labeling for each species is detailed in
901 the STAR methods.

902 B. Average NC ratio (with error bars representing the standard deviation) for all the included
903 species.

904 See also Figures S6-7.

905

906 **Figure 5. The average NC ratio is linked to the average cell size.**

907 For all plots, error bars indicate 95% confidence intervals.

908 A. Scatter plot of average cell volume versus average NC ratio for all the included species.
909 Abbreviated species names are indicated next to the corresponding datapoint; see Key Resources
910 Table for a full name description. Inset: same relationship with average cell volume on a
911 logarithmic scale.

912 B. Scatter plot of average NC ratio versus average cell length, average cell width, average cell area
913 or average surface area to volume ratio.

914

915 **Figure 6. The intracellular mobility of large objects displays non-linear dynamics and is**
916 **different between *E. coli* and *C. crescentus*.**

917 *E. coli* cells (CJW6723) were grown in M9 medium supplemented with 0.2% glycerol and *C.*
918 *crescentus* cells (CJW6917) in M2 medium supplemented with 0.2% glucose, resulting in similar
919 doubling times of ~120 min.

920 A. Frequency distributions of GFP- μ NS spot intensities in *E. coli* (n= 2279) and *C. crescentus* (n =
921 2019) cells. Three bins of GFP- μ NS particles with similar intensities and thus sizes are indicated
922 in color.

923 B. Ensemble-averaged MSDs of GFP- μ NS particles (belonging to the intensity bins highlighted in
924 panel A) in *E. coli* cells (n = 1208, 600 and 200 for bins 1, 2 and 3, respectively) and *C. crescentus*

925 cells ($n = 837, 984$ and 374 for bins 1, 2 and 3, respectively). Error bars indicate 95% confidence
926 intervals.

927 C. Ensemble-averaged MSDs of fluorescently-labeled ribosomes in *E. coli* (SX289) and *C.*
928 *crenscentus* (CJW5156) at different acquisition frame intervals. For each frame interval, > 8900
929 trajectories were collected. Only the first four points of the MSDs are shown for each frame
930 interval. Error bars indicate 95% confidence intervals.

931 D. Same as panel C, except that ensemble-averaged MSDs from rifampicin-treated cells (200
932 $\mu\text{g/ml}$, 2 h) were added for comparison to the results shown in panel A. For each frame interval,
933 > 3700 trajectories were collected in rifampicin-treated cells. For these MSDs, only the first six
934 points are shown for the 5 ms and 30 ms frame intervals. The color scheme for the frame intervals
935 is the same as in C. Error bars indicate 95% confidence intervals.

936 E. Plot showing the apparent diffusion coefficients calculated from the aforementioned MSDs as
937 a function of the frame interval. Error bars indicate 95% confidence intervals.

938 F. Same as E, but for the anomalous exponent.

939 G. Representative plots showing the evolution of the ribosomal fluorescence recovery over time
940 (up to 450 s) along the length of a cephalixin-treated *E. coli* cell (CJW4677) and of an FtsZ-
941 depleted *C. crescentus* cell (CJW3821) following photobleaching of about half of the cell. The
942 dotted line shows the fluorescence profile prior to bleaching.

943 See also Figure S8.

944

945 **Figure 7. The spatial organization of ribosomes in bacteria is linked to the average NC ratio**
946 **and cell size.**

947 A. Top, representative fluorescence images of *E. coli* cells (CJW6769) grown in M9 medium
948 supplemented with 0.2% glycerol (M9gly) or 0.2% glucose, 0.1% casamino acids and $1\mu\text{g/ml}$
949 thiamine (M9gluCAAT). Bottom, fluorescence intensity profiles of DAPI and RpsB-mEos2 signals
950 for these cells.

951 B. Scatter plot of average SCF versus average NC ratio for *E. coli* cells (CJW6769) grown in the
952 indicated growth media (for a full description of the growth media, see Table S1). The SCF was
953 calculated by comparing the correlation between the DAPI and the RpsB-mEos2 signals for the
954 indicated species. Error bars indicate 95% confidence intervals.

955 C. Representative phase contrast and fluorescence images of *E. coli* cells (CJW4677) after the FISH
956 procedure, highlighting the correspondence between the use of RplA-GFP and FISH (targeting
957 16S ribosomal RNA with the Cy5-labeled EUB338 probe) for visualizing ribosome localization.
958 Cells were grown in M9 medium supplemented with 0.2% glycerol, 0.1% casamino acids, and
959 $1\mu\text{g/ml}$ thiamine.

960 D. Fluorescence intensity profiles of DAPI, RplA-GFP, and rRNA FISH (Cy5-EUB338) signals of *E.*
961 *coli* cells (CJW4677) indicated in C, grown in M9 medium supplemented with 0.2% glycerol, 0.1%
962 casamino acids, and 1 µg/ml thiamine.

963 E. Frequency distributions of SCF values between the rRNA FISH (Cy5-EUB338), RplA-GFP, and
964 DAPI signals.

965 F. Scatter plots of average SCF versus average NC ratio (left) or versus average cell area (right).
966 The SCF was calculated by comparing the correlation between the DAPI and the rRNA FISH (Cy5-
967 EUB338) signals for the indicated species. Error bars indicate 95% confidence intervals.

968 See also Figure S8.

969

970 **STAR Methods**

971

972 **CONTACT FOR REAGENT AND RESOURCE SHARING**

973 Further information and requests for resources and reagents should be directed to and will be
974 fulfilled by the Lead Contact, Christine Jacobs-Wagner (Christine.Jacobs-Wagner@yale.edu).

975

976 **EXPERIMENTAL MODEL AND SUBJECT DETAILS**

977 ***Bacterial strains and growth conditions***

978 Construction of strains and plasmids is detailed in Table S2.

979

980 To obtain steady-state growth conditions, cells were first inoculated in the appropriate growth
981 medium and grown to stationary phase in culture tubes. Cells were subsequently re-inoculated
982 into fresh medium by diluting them 1/10000 or more, and grown until they reached an optical
983 density at 600 nm (OD₆₀₀) of 0.1-0.3 (depending on the growth medium and organism) before
984 sampling for microscopy.

985

986 *E. coli* cells were grown in LB medium (30 °C), gut microbiota medium (GMM; 30 °C) (Goodman
987 et al., 2011) or M9 medium (37 °C) supplemented with 0.2% carbon source and, in certain
988 instances, with 0.1% casamino acids and 1 µg/ml thiamine (CAAT). *C. crescentus* cells were grown
989 at 30 °C either in PYE medium or M2G medium. *Sinorhizobium meliloti* (30 °C), *Pseudomonas*
990 *syringae* (30 °C), *Janthinobacterium lividum* (25 °C), and *Burkholderia thailandensis* (30 °C) were
991 grown in LB medium. *Rhizobium leguminosarum*, *Agrobacterium tumefaciens*, *Asticcacaulis*
992 *excentricus*, *Chryseobacterium indologenes*, *Brevundimonas subvibrioides*, *Brevundimonas*
993 *bacteroides*, and *Brevundimonas diminuta* were grown at 30 °C in PYE medium. *Vibrio harveyi* and
994 *Vibrio fischeri* were grown at 30 °C in LBS medium. *Myxococcus xanthus* and *Flavobacterium*

1031 controlled by the Nikon Elements software. The following Chroma filter sets were used to acquire
1032 fluorescence images: DAPI (excitation ET350/50x, dichroic T400lp, emission ET460/50m), CFP
1033 (excitation ET436/20x, dichroic T455lp, emission ET480/40m), GFP (excitation ET470/40x,
1034 dichroic T495lpxr, emission ET525/50m), YFP (excitation ET500/20x, dichroic T515lp, emission
1035 ET535/30m), mCherry/TexasRed (excitation ET560/40x, dichroic T585lpxr, emission
1036 ET630/75m) and Cy5.5 (excitation ET650/45x, dichroic T685lpxr, emission ET720/60m).
1037 Specialized microscopy setups used for FRAP experiments and single-molecule or single-particle
1038 tracking are detailed below.

1039

1040 ***GFP- μ NS experiments***

1041 For GFP- μ NS experiments in *E. coli*, we used a published protocol (Parry et al., 2014). Briefly, *E.*
1042 *coli* strain CJW6723 was grown at 30 °C in M9 medium supplemented with 0.2% glycerol to an
1043 OD₆₀₀ = 0.05-0.1. The synthesis of GFP- μ NS was induced by the addition of 200-500 μ M IPTG for
1044 60-120 min. After induction, cells were spun down (5000 x g for 5 min) and washed with fresh
1045 M9 glycerol medium and grown for at least 60 min to allow for GFP maturation. For experiments
1046 in *C. crescentus*, strain CJW6723 was grown at 30 °C in M2 medium supplemented with 0.2%
1047 glucose to an OD₆₆₀ = 0.05-0.1. GFP- μ NS synthesis was induced by the addition of 0.3% xylose to
1048 the medium for 30-120 min. After induction, cells were spun down and washed with fresh M2G
1049 medium and grown for at least 60 min to allow for GFP maturation. Cells were then spotted on
1050 1.5% agarose pads containing M9 glycerol (*E. coli*) or M2G (*C. crescentus*) and imaged every 2 s at
1051 30 °C.

1052

1053 ***Photoactivated localization and single-molecule tracking experiments***

1054 For photoactivated localization microscopy and single-molecule (ribosome) tracking, cover slips
1055 and glass slides were washed in the following manner: sonication in 1 M KOH (15 min), sonication
1056 in milliQ H₂O (15 min) and sonication in 70% ethanol (15 min) with 3-5 milliQ H₂O rinses between
1057 wash solution changes. Cleaned glass slides and cover slips were then dried with pressured air.
1058 Cells were spotted on a 1.5% agarose pad made with M9 medium supplemented with 0.2%
1059 glycerol, 0.1% casamino acids, and 1 μ g/ml thiamine for *E. coli* or M2 medium supplemented with
1060 0.2% glucose for *C. crescentus*. Imaging was performed with an objective heat ring set at 30 °C. All
1061 images were acquired on an N-STORM microscope (Nikon) equipped with a CFI Apo TIRF 100 \times
1062 oil immersion objective (NA 1.49), lasers (Agilent Technologies) emitting at 405 nm (0.1-10%)
1063 and 561 nm (15-100%), and a built-in Perfect Focus system. Raw single-molecule data were taken
1064 at a frame rate of 200 to 10 frames per second in a field of view of 36 \times 36, 120 \times 120, or 200 \times
1065 200 pixels (depending on the frame rate) with an Andor iXon X3 DU 897 EM-CCD camera (Andor

1066 Technology). Rifampicin treatment was performed by exposing cells to 200 µg/ml (*E. coli*) or 50
1067 µg/ml (*C. crescentus*) rifampicin for 2 h in liquid culture before sampling and imaging.

1068

1069 ***Fluorescence recovery after photobleaching experiments***

1070 For the FRAP experiments, filamentous cells (generated either by a 2 h treatment with 50 µg/ml
1071 cephalixin for *E. coli* or a 3-6 h FtsZ depletion in *C. crescentus*) were spotted on 1.5% agarose pads
1072 with M9 medium supplemented with 0.2% glycerol, 0.1% casamino acids, and 1 µg/ml thiamine
1073 or PYE. Cells were imaged at room temperature (~22 °C) with a Nikon E80i microscope equipped
1074 with 100X Plan Apo 1.45 NA phase contrast objective and an Andor iXonEM+ DU-897 camera
1075 controlled by the Metamorph software. Fluorescence photobleaching was performed using a
1076 Photonic Instrument Micropoint laser system at 488 nm. Cells were imaged once before
1077 photobleaching, then bleached (for ~0.5 s), and subsequently imaged at equal intervals (3-6 s for
1078 450 s depending on whether *E. coli* or *C. crescentus* was imaged).

1079

1080 ***Fluorescence in situ hybridization experiments***

1081 For FISH experiments, *E. coli* cells were grown in LB medium at 30 °C, *C. crescentus* cells were
1082 grown in PYE medium at 30 °C, and the other bacterial species were grown as described above.
1083 FISH was performed similarly to previous methods described by our laboratory (Kim and Jacobs-
1084 Wagner, 2018; Montero Llopis et al., 2010). Briefly, exponentially growing cells ($OD_{600} < 0.3$) were
1085 fixed in a 4% formaldehyde solution (4% formaldehyde, 30 mM NaHPO₃ pH 7.5) for 15 min at
1086 room temperature followed by 30 min on ice. The samples were spun down (5000 x g for 3 min)
1087 and washed in phosphate-buffered saline (PBS) treated with diethyl pyrocarbonate (DEPC) 3
1088 times. The cell pellets were resuspended in DEPC-treated PBS (8.0 g/l NaCl, 0.2 g/l KCl, 1.44 g/l
1089 Na₂HPO₄ and 0.24 g/l KH₂PO₄) and adhered to poly-L-lysine-coated coverslips. Cells were then
1090 lysed with 70% ethanol for 5 min at room temperature. Pre-hybridization was then performed
1091 with a 40% formamide, 2x saline-sodium citrate solution (SSC, 300 mM NaCl, 30 mM sodium
1092 citrate, pH 7.0) containing 0.2 mM vanadyl ribonucleoside complex (VRC) for 2 h at 37 °C.
1093 Immediately afterwards, hybridization was performed with EUB338 (5'-
1094 GCTGCCTCCCGTAGGAGT-3', 5'-monolabeled with Cy5) in a solution containing 4 nM EUB338,
1095 40% formamide, 2x SSC, 0.2 mM VRC, 10% dextran sulfate, 0.1% bovine serum albumin, and 0.4
1096 mg/ml *E. coli* tRNA. Hybridization proceeded for 16 h at 37 °C and was then washed 5 x with wash
1097 solution (50 % formamide, 2x SSC) and 10x with DEPC-treated PBS. Finally, 1 µg/ml DAPI was
1098 added to the coverslip, which was then mounted on a glass slide for imaging.

1099

1100

1101

1102 **DNA dye labeling**

1103 For live cells, the nucleoid was visualized by incubating 1 µg/ml DAPI with cells in their growth
1104 medium for 10 min. Due to a lack of labeling efficiency with DAPI in live cells of some of the species
1105 that were studied, all species for Figures 4 and 5 (with the exception of *E. coli* in different
1106 conditions) were fixed with 4% formaldehyde for 15 min at room temperature and 30 min on ice.
1107 They were then washed three times with 1 x PBS and spun down at 7000 rpm. Fixed *A. excentricus*,
1108 *A. tumefaciens*, *B. subvibrioides*, *C. algicola*, *C. hutchinsonii*, *H. rosenbergii*, *B. bacteroides*, *B.*
1109 *diminuta*, *C. indologenes*, *F. johnsoniae*, *M. xanthus*, *P. syringae*, *R. leguminosarum*, *S. meliloti* and *C.*
1110 *crescentus* were stained with 1 x SYBR Green. Fixed *B. theta*, *B. ovatus*, *V. harveyi* and *P. distasonis*
1111 were stained with 1 µg/mL DAPI. Fixed *B. megaterium*, *C. violaceum*, *J. lividum*, *V. fischeri*, *B.*
1112 *subtilis*, *B. thailandensis*, *E. coli*, *Anaerostipes sp.*, *B. xylanisolvens*, *C. aerofaciens*, *C. hathewayi*, *L.*
1113 *reuteri*, *P. alcalifaciens*, *R. intestinalis*, *C. boltae*, *L. sphaericus* and *P. polymyxa* were stained with 1
1114 µg/ml Hoechst 33342.

1115

1116 **Image processing**

1117 Cell outlines were generated using the open-source image analysis software Oufiti (Paintdakhi et
1118 al., 2016). Nucleoids were detected using Oufiti's objectDetection module. For comparison
1119 purposes, we used the same nucleoid detection parameters for all image datasets (see
1120 Supplemental Information for parameters), with a single exception (see below). The resulting cell
1121 lists were further processed and analyzed in MATLAB (Mathworks) using custom-built
1122 algorithms (see below).

1123

1124 One experiment required optimizing our nucleoid detection pipeline. Elongation of *dnaC2* cells
1125 under restrictive conditions (related to Figure 2C-D) led to a decrease in the fraction of nucleoid-
1126 bound HU-mCherry signal. To overcome this, we used an adjusted nucleoid detection function:
1127 Nucleoid_Detection_High_Background.m that uses MATLAB built-in functions to threshold and
1128 identify nucleoids within Oufiti cell meshes.

1129

1130 SeqA-mCherry signal information was added to *E. coli* cell lists using the MATLAB function
1131 Add_SeqA_Area.m (see Supplemental Information for the code). DnaN-CFP information was
1132 added to *C. crescentus* cell lists using the MATLAB function Add_DnaN_Area.m.

1133

1134 **Support Vector Machine model for curation of cell contours**

1135 In similar fashion as before (Campos et al., 2018), we used an automated approach to identify
1136 poor and incorrect cell detections across our datasets. We trained a support vector machine
1137 (SVM) model based on 11 normalized phase-contrast features: cell length, cell volume, integrated

1138 phase signal, mean cell contour intensity, minimum cell contour intensity, maximum curvature of
1139 cell contour, minimum inflated cell contour intensity, mean intensity gradient across the cell
1140 contour, maximum variability in contour intensity, mean variability in contour intensity and
1141 maximum cell pixel intensity. We visually scored 20,265 cells and used 30% of them (6,080 cells)
1142 to train the SVM model. The model was evaluated using a k-fold cross-validation approach,
1143 leading to a generalized misclassification rate of 9.9%. We used the remaining 70% of the dataset
1144 (14,185 cells) to validate the model. The SVM classifier achieves a balanced classification rate of
1145 90.9% and features an AUROC of 0.9640.

1146

1147 The SVM model underperformed for species (e.g., *C. crescentus*) and mutants (e.g., *dnaC2* at the
1148 restrictive temperature) with morphologies that deviated significantly from *E. coli*'s typical rod
1149 shape. Therefore, in these instances, we resorted to visual inspection and curation of the obtained
1150 cell contours. For time-lapse experiments, visual inspection and manual curation of the cell
1151 contours was also required.

1152

1153 ***Growth rate measurements***

1154 Growth rates were measured in 96-well plates in a Synergy2 microplate reader (BioTek). Cultures
1155 were first grown to stationary phase and re-inoculated into 150 μ l fresh medium (1/300).
1156 Cultures were subsequently grown for 60 h at 37 °C with OD₆₀₀ measurements every 4 min. The
1157 maximal growth rate was extracted from the obtained growth curves by fitting the Gompertz
1158 function (Zwietering et al., 1990).

1159

1160 ***Osmolality measurements***

1161 Osmolality of growth media was measured using a Precision Systems 6002 Touch Micro
1162 OSMETTE™ osmometer, which uses the freezing point method for osmolality measurements. All
1163 measurements were conducted in duplicate.

1164

1165 **QUANTIFICATION AND STATISTICAL ANALYSIS**

1166 ***Cellular characteristics***

1167 Properties of individual cells (cell and nucleoid dimensions, DAPI fluorescence intensity,
1168 fluorescent marker behavior, etc.) were extracted from cell lists obtained from Oufiti using the
1169 MATLAB function Extract_Cell_Properties.m. Morphological features (e.g., cell length, width, area,
1170 and volume) were determined by summing the dimensions of each individual segment of the cell
1171 mesh identified by Oufiti. See <https://oufti.org/> for more details.

1172

1173

1174 ***Correlation coefficients***

1175 Kendall correlation coefficients between variables were calculated using MATLAB's built-in corr
1176 function.

1177

1178 ***Unconstrained linear fits***

1179 Unconstrained linear fits were performed using MATLAB's built-in polyfit function.

1180

1181 ***Nucleoid exclusion of ribosomes***

1182 The extent of ribosome exclusion was determined by calculating the signal correlation factor
1183 (SCF) between the DNA and ribosome signals. For each individual cell, the SCF was calculated by
1184 examining a specific "correlation area", corresponding to an intracellular region determined by
1185 two user-specified parameters. The restriction of the calculation to this area was required to
1186 ensure optimal correlation calculations for cells with different shapes and sizes as the smaller
1187 cytoplasmic volume at the cell poles and the cell periphery leads to a general decrease in
1188 fluorescent signal which, in turn, artificially generates positive biases in the calculation of the SCF.
1189 The first parameter was the number of pixels, starting from the cell poles, to exclude from the
1190 calculation. The second parameter was the number of pixels, starting from the cell centerline, to
1191 include in the calculation. Together, these parameters defined the correlation region for which
1192 the correlation between pixel values was determined. Different combinations of these two
1193 parameters were scanned for each growth condition and species, and parameters were chosen
1194 by finding the minimal average SCF. The minimal average SCF was selected to avoid the positive
1195 SCF biases introduced by the cell poles and periphery. The following MATLAB functions were
1196 used for this analysis: Pixel_Correlation_Multiple_Experiments_Scan.m,
1197 Pixel_Correlation_Parallel.m, Cell_Pixel_Correlation.m, Extract_Cell_Pixels.m, Cell_Projection.m
1198 and Taylor_Smooth.m.

1199

1200 ***Mean squared displacements of single ribosomal particles***

1201 Particle locations determined using the *uTrack* package (Jaqaman et al., 2008) were linked into
1202 trajectories based on a previously described algorithm (Crocker and Grier, 1996). Briefly, the
1203 most likely trajectories were constructed by minimizing the sum of squared particle
1204 displacements between two consecutive frames. Trajectories of lengths smaller than five
1205 displacements were removed. Mean squared displacements (MSD) at various time delays were
1206 then calculated from individual trajectories. For each frame interval, an ensemble-averaged MSD
1207 was obtained by averaging individual MSD curves weighted by the corresponding trajectory
1208 lengths. For each MSD curve, the slope was determined by fitting the three smallest time delays
1209 using least squares regression and by further dividing by a factor of 4 to obtain the apparent

1210 diffusion coefficient D_a . Similarly, the slope of the log-log MSD curve was determined by fitting
1211 the three smallest time delays to obtain the anomalous exponent α . Due to the short average
1212 trajectory length, only the three smallest time delays were used to ensure reliable determinations
1213 of these values.

1214

1215 ***Mean squared displacements of GFP- μ NS particles***

1216 Cell meshes obtained from Oufiti were used to limit particle localization to the region within cells
1217 and prevent spurious trajectory linking between cells. Particle localization was performed using
1218 the function `uNS_Particle_Tracking.m` to fit a 2D Gaussian to filtered images.

1219

1220 **DATA AND SOFTWARE AVAILABILITY**

1221 All computer code is provided in the Supplemental Information and can also be found at
1222 <https://github.com/JacobsWagnerLab/published>.

1223

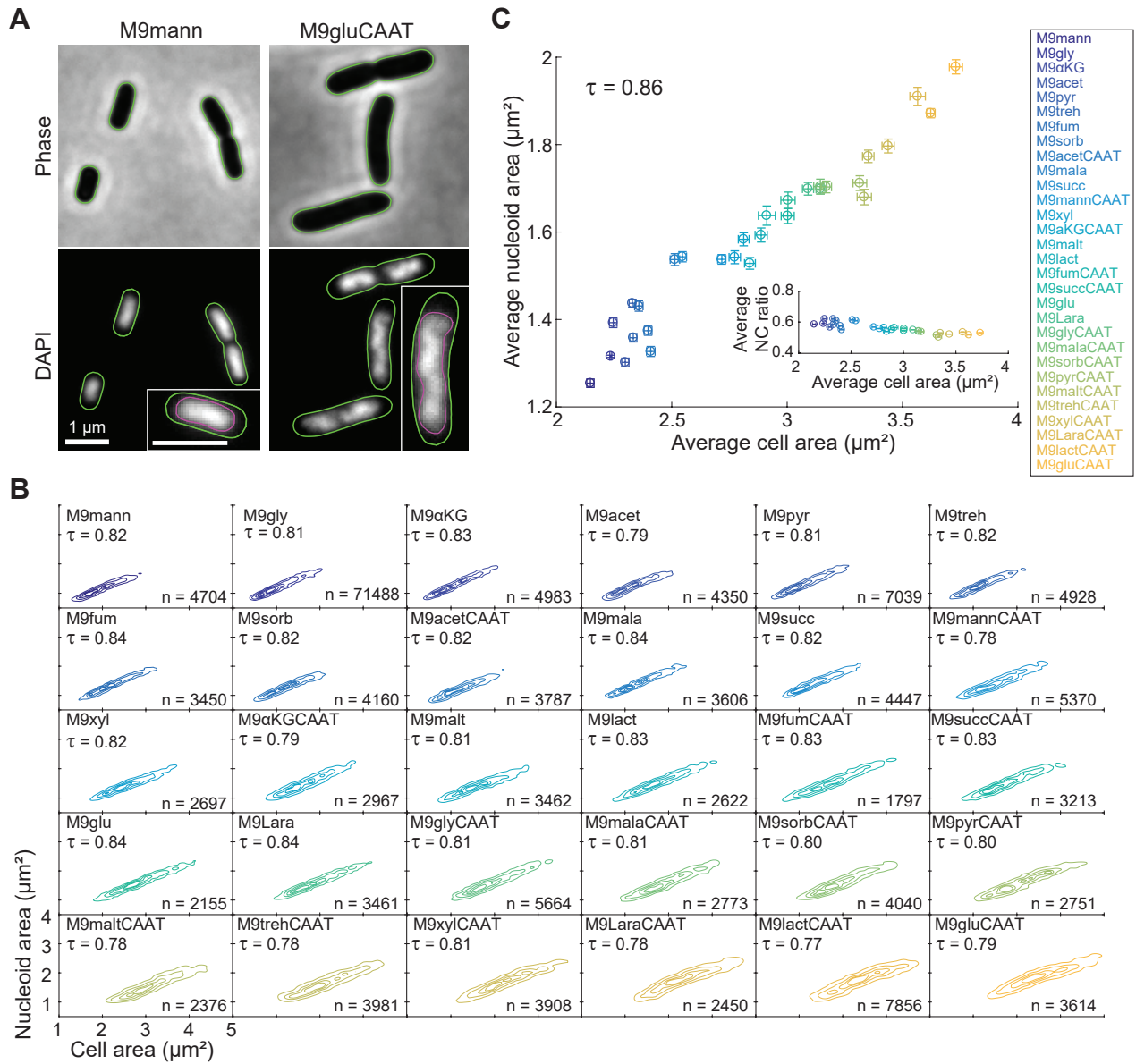


Figure 1

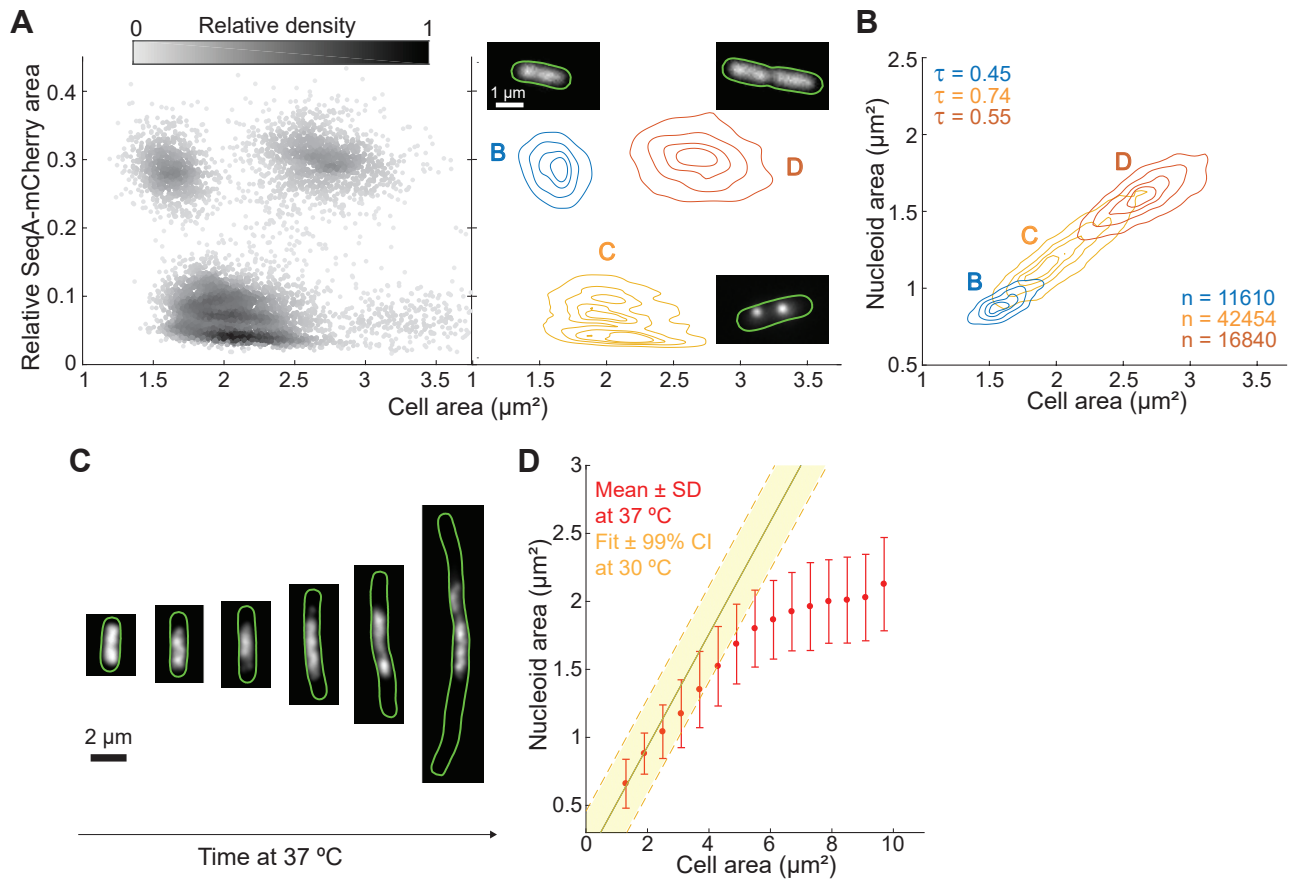


Figure 2

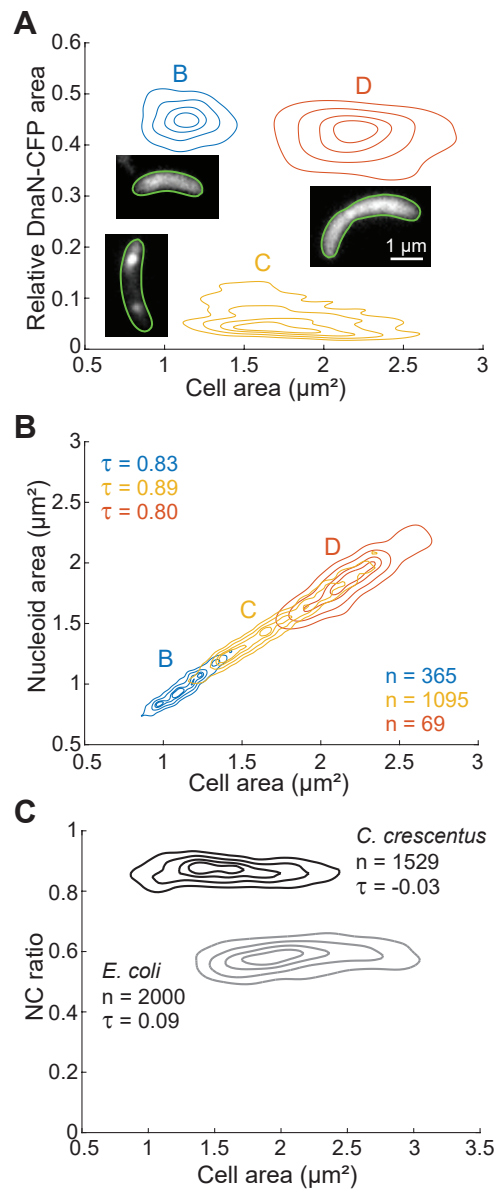


Figure 3

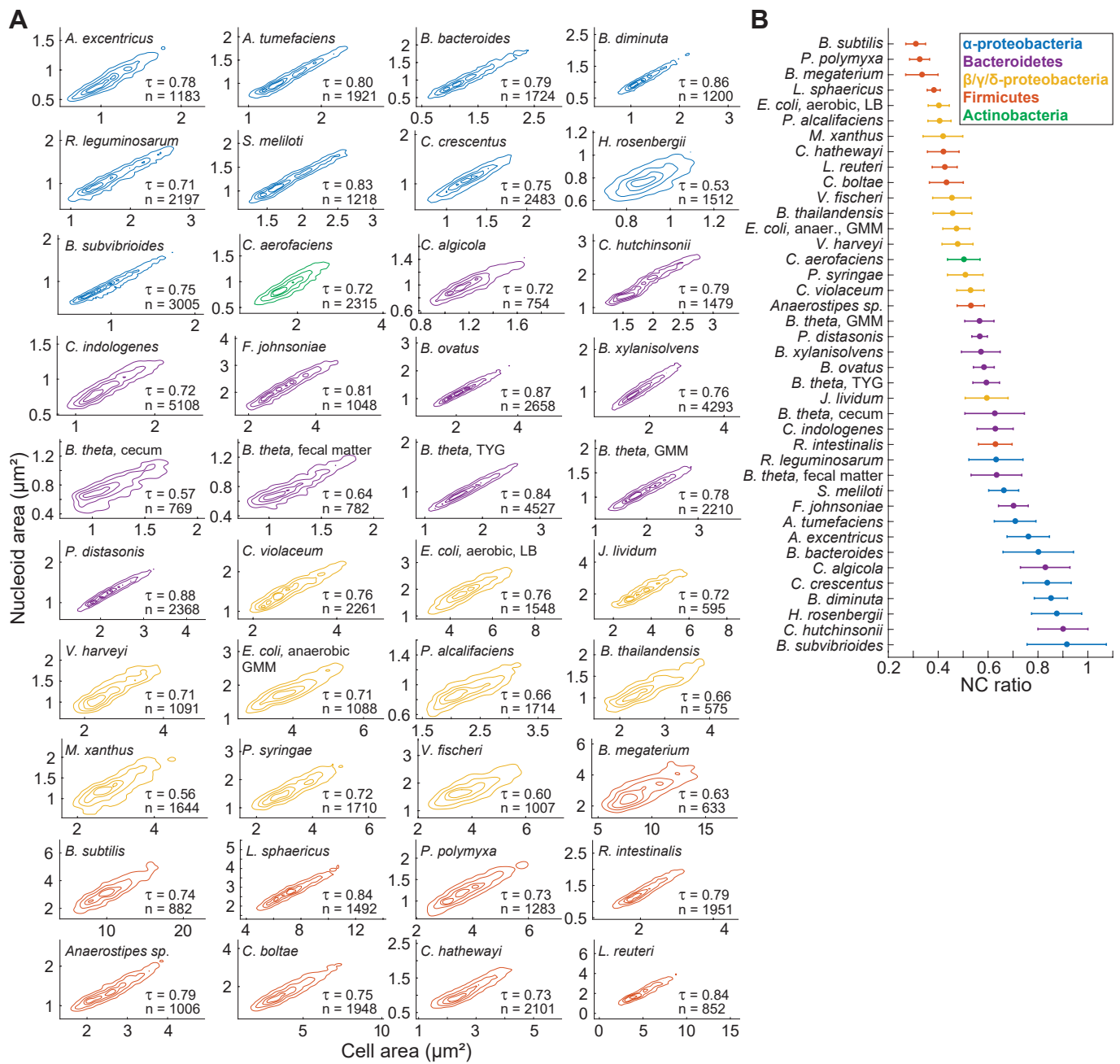


Figure 4

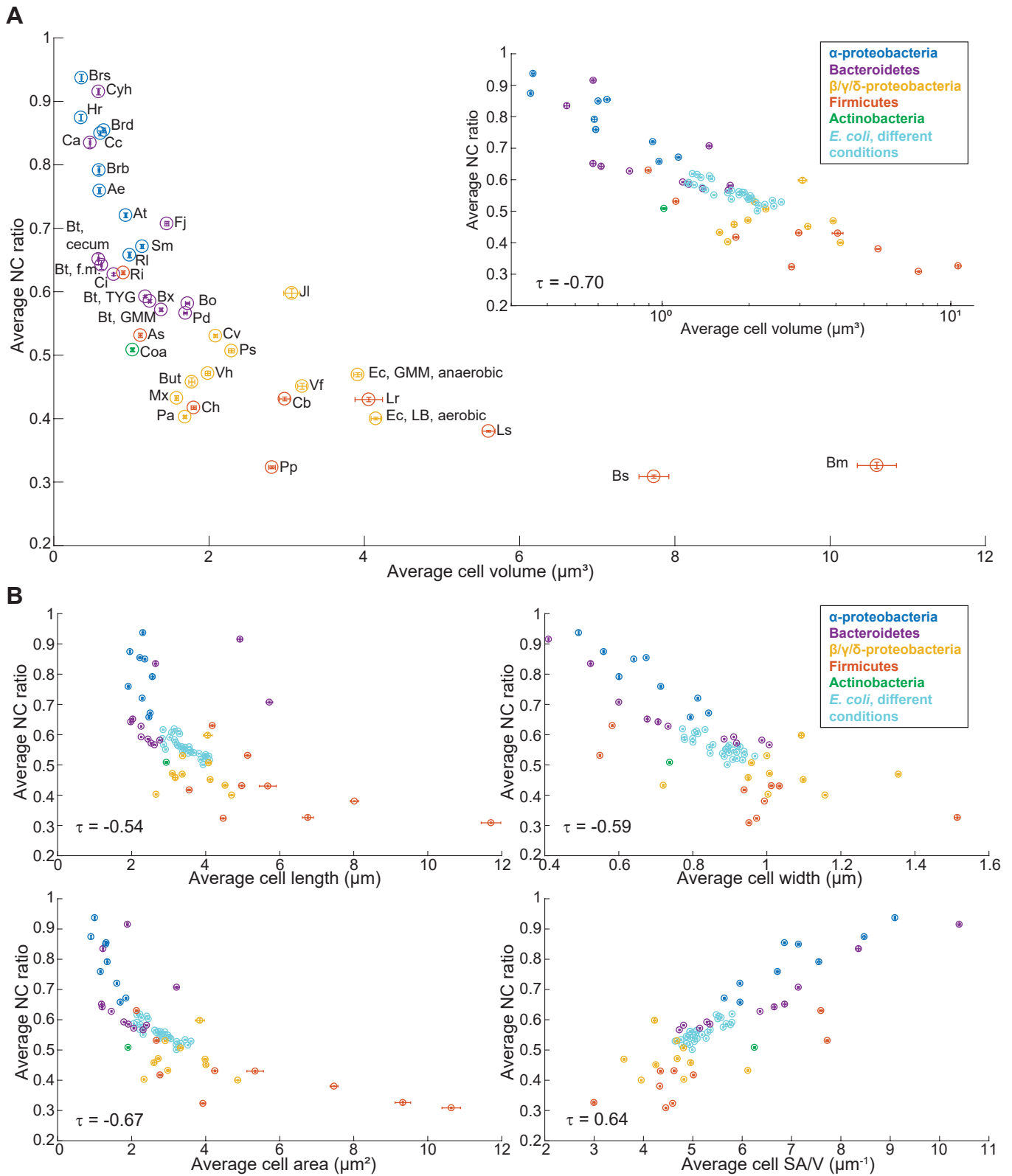


Figure 5

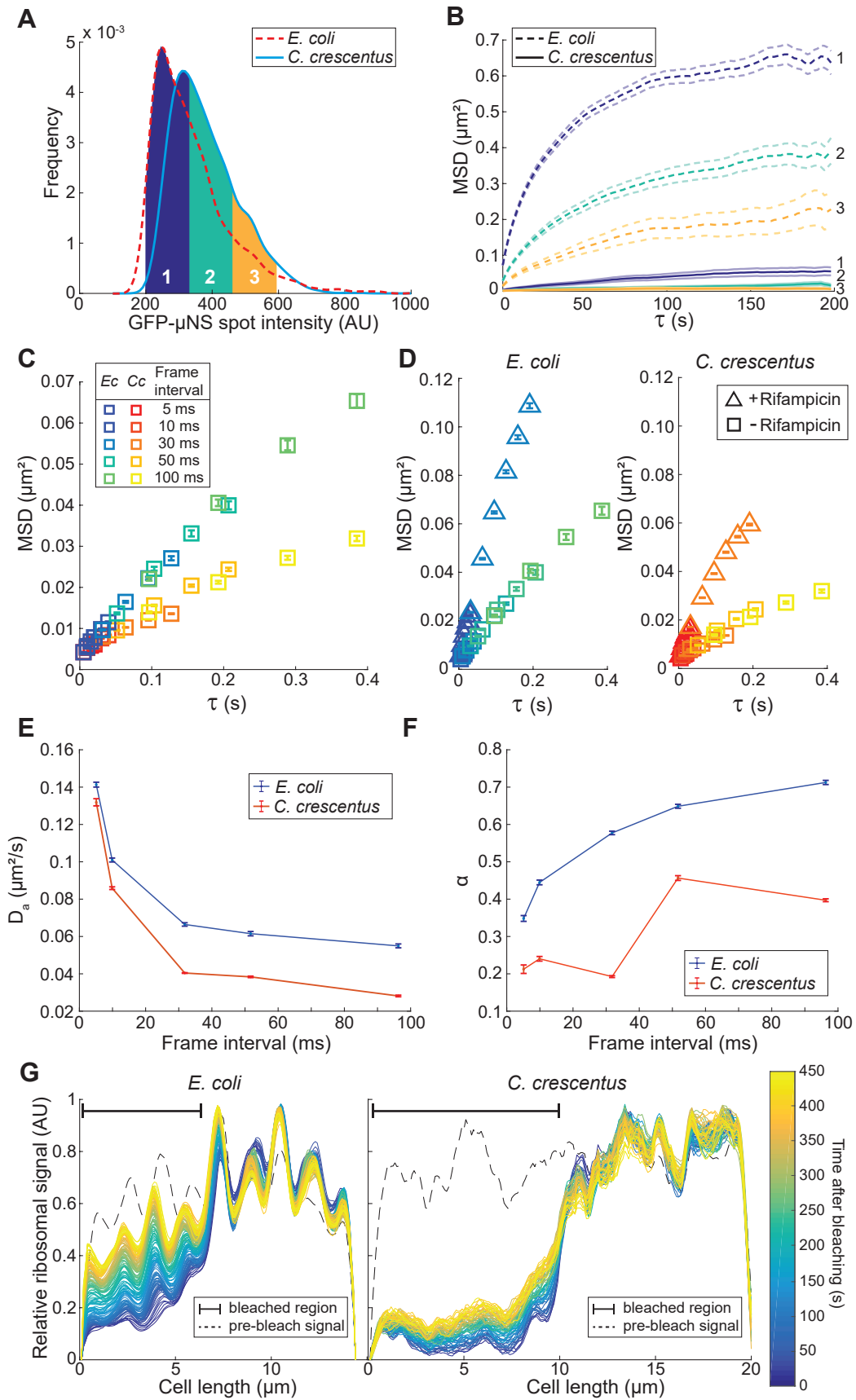


Figure 6

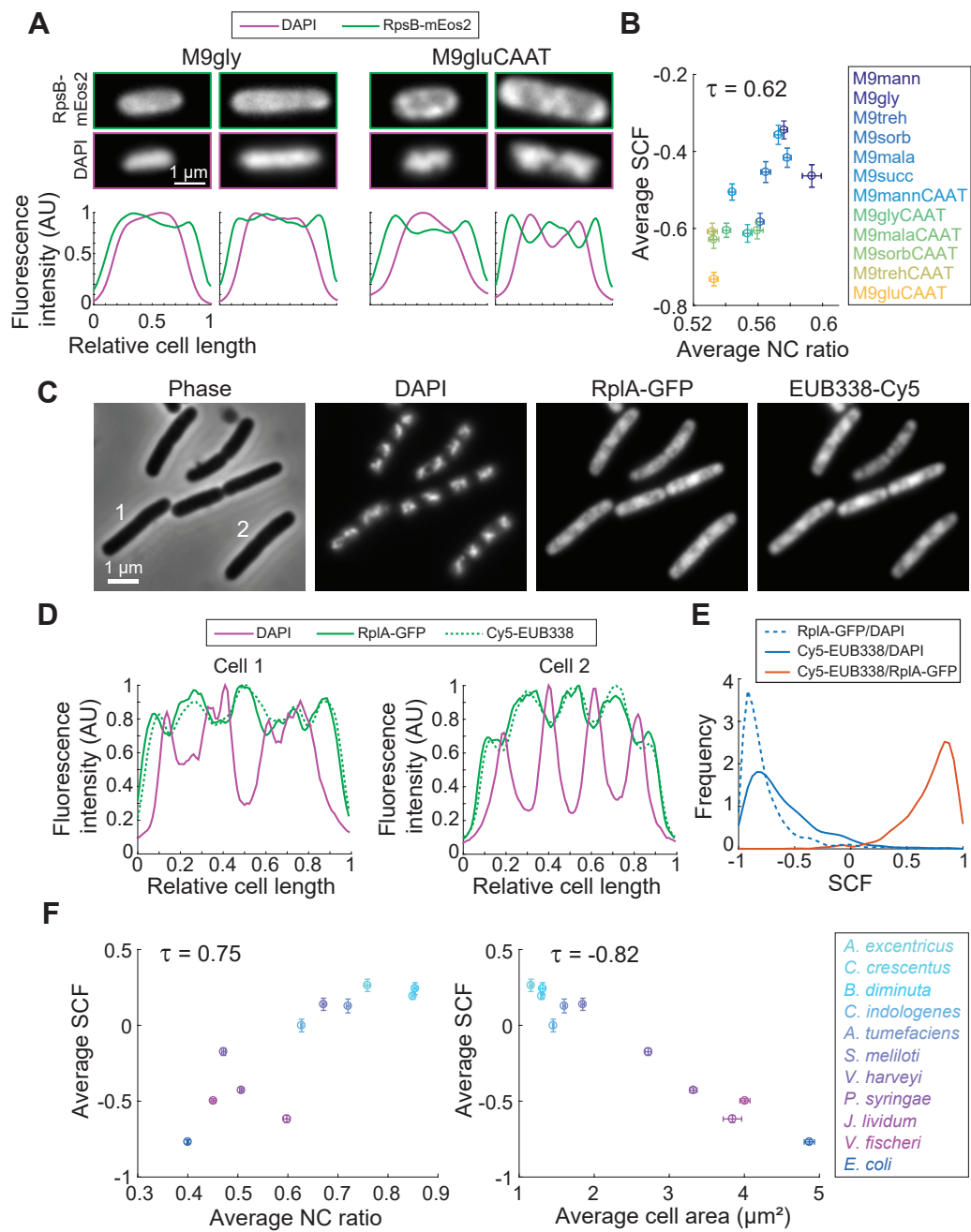


Figure 7